nature biomedical engineering

ARTICLES

https://doi.org/10.1038/s41551-019-0498-9

Quantitative prediction of human pharmacokinetic responses to drugs via fluidically coupled vascularized organ chips

Anna Herland[1,2,3,11], Ben M. Maoz[1,4,5,6,11], Debarun Das[7,11], Mahadevabharath R. Somayaji[7,11], Rachelle Prantil-Baun[1,11], Richard Novak[1,11], Michael Cronce[1], Tessa Huffstater[1], Sauveur S. F. Jeanty[1], Miles Ingram[1], Angeliki Chalkiadaki[1], David Benson Chou[1], Susan Marquez[1], Aaron Delahanty[1], Sasan Jalili-Firoozinezhad[1,8], Yuka Milton[1], Alexandra Sontheimer-Phelps[1,9], Ben Swenor[1], Oren Levy[1], Kevin K. Parker[1,4], Andrzej Przekwas[7] and Donald E. Ingber[1,2,10*]

Analyses of drug pharmacokinetics (PKs) and pharmacodynamics (PDs) performed in animals are often not predictive of drug PKs and PDs in humans, and in vitro PK and PD modelling does not provide quantitative PK parameters. Here, we show that physiological PK modelling of first-pass drug absorption, metabolism and excretion in humans—using computationally scaled data from multiple fluidically linked two-channel organ chips—predicts PK parameters for orally administered nicotine (using gut, liver and kidney chips) and for intravenously injected cisplatin (using coupled bone marrow, liver and kidney chips). The chips are linked through sequential robotic liquid transfers of a common blood substitute by their endothelium-lined channels (as reported by Novak et al. in an associated Article) and share an arteriovenous fluid-mixing reservoir. We also show that predictions of cisplatin PDs match previously reported patient data. The quantitative in-vitro-to-in-vivo translation of PK and PD parameters and the prediction of drug absorption, distribution, metabolism, excretion and toxicity through fluidically coupled organ chips may improve the design of drug-administration regimens for phase-I clinical trials.

The high failure rate of drugs in clinical trials is in part due to fundamental interspecies differences between humans and the animals that are used in preclinical testing; these difference often lead to incorrect predictions of critical human pharmacokinetics (PKs) and pharmacodynamics (PDs) parameters (such as clearance, safety margins, toxicity and efficacy)[1]. Isolated cells from relevant organs (such as hepatocytes from liver) and organ-specific cell cultures have been used for in vitro–in vivo correlation or extrapolation of certain drug compound and PK properties (such as hepatic clearance), but these approaches do not reliably or quantitatively predict human PK parameters or PD responses[2,3]. One potential way to confront this challenge is to use cultures of human organ-specific cells in microfluidic devices, transfer fluids between them, and analyse drug levels, cell-specific markers and metabolism in vitro[4–8]. Qualitative predictions of some drug toxicity responses have been generated using PK/PD models with such multiphysiological systems (including liver, lungs and kidneys)[9–13], but they have not been able to quantitatively translate in vitro results into in vivo PK parameters (IVIVT). Moreover, the physiological relevance of these results is unclear as the drug-containing medium in these devices flows directly from one parenchymal tissue type to another (for example, from hepatocytes to lung epithelium) without passing through the endothelial tissue barrier that is crucial for defining drug PK behaviour in vivo[6]. Manual transfer of fluid between cultured intestine, liver, kidney, skeletal muscle and blood–brain barrier microfluidic systems (only some of which contained endothelium-lined channels) combined with PK/PD modelling resulted in organ-specific processing of drug metabolism and barrier penetrance that were consistent with clinical data[14]; however, these results did not result in quantitative physiologically based PK (PBPK) predictions, which are needed by the clinical and pharmaceutical communities for meaningful compound assessment or design of optimal clinical drug administration regimens due to the lack of physiologically relevant organ–organ linking.

A multi-organ-chip first-pass metabolism model

To address this challenge, we created a first-pass model of human drug absorption, metabolism and excretion by fluidically coupling two-channel, microfluidic, human organ-chip models of the gut, liver and kidneys[15–17] through their vascular endothelium-lined channels, which are separated by a porous extracellular-matrix-coated membrane from parallel channels lined by human organ-specific parenchymal cells, and integrating an arteriovenous (AV) reservoir into the fluid path to enable drug mixing (Fig. 1a, Supplementary Tables 1 and 2; see Methods). The AV reservoir is a key design feature because it mimics the compartment that

[1]Wyss Institute for Biologically Inspired Engineering, Harvard University, Boston, MA, USA. [2]Division of Micro and Nanosystems, KTH Royal Institute of Technology, Stockholm, Sweden. [3]AIMES, Department of Neuroscience, Karolinska Institute, Stockholm, Sweden. [4]Harvard John A. Paulson School of Engineering and Applied Sciences, Harvard University, Cambridge, MA, USA. [5]Department of Biomedical Engineering, Tel Aviv University, Tel Aviv, Israel. [6]Sagol School of Neuroscience, Tel Aviv University, Tel Aviv, Israel. [7]CFD Research Corporation, Huntsville, AL, USA. [8]Department of Bioengineering and Institute for Bioengineering and Biosciences, Instituto Superior Técnico, Portugal Graduate Program, Universidade de Lisboa, Lisbon, Portugal. [9]Faculty of Biology, University of Freiburg, Freiburg, Germany. [10]Vascular Biology Program and Department of Surgery, Boston Children's Hospital and Harvard Medical School, Boston, MA, USA. [11]These authors contributed equally: Anna Herland, Ben M. Maoz, Debarun Das, Mahadevabharath R. Somayaji, Rachelle Prantil-Baun, Richard Novak. *e-mail: don.ingber@wyss.harvard.edu

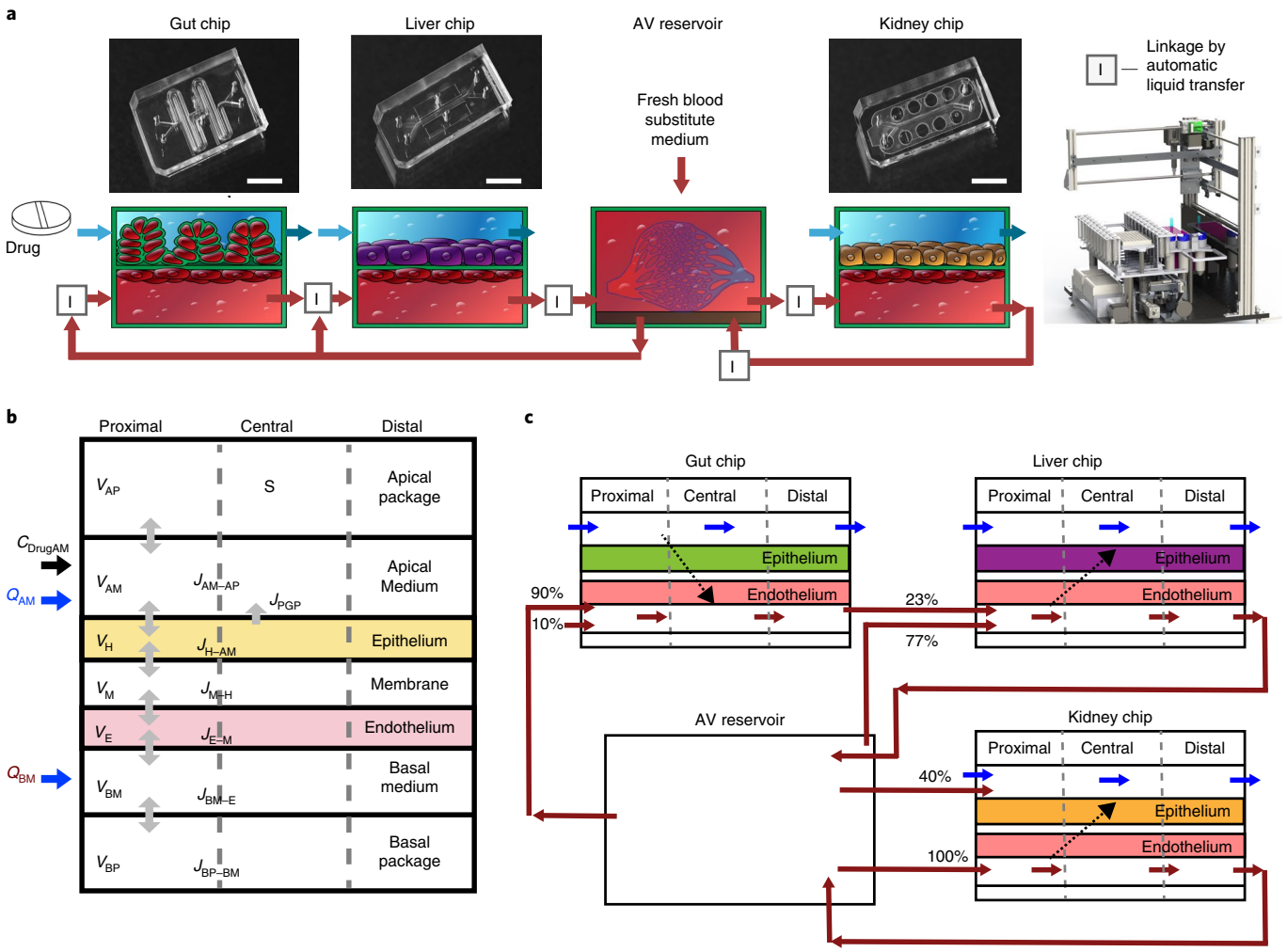

Fig. 1 | Development of a first-pass multi-organ-chip system. a, Top: photographs of the organ chips. Scale bars, 5 mm. Bottom: diagrams of the gut, liver and kidney chips—which contain apical parenchymal and basal vascular compartments separated by a porous matrix-coated membrane—indicating the manner in which the chips are fluidically linked to each other and to the AV reservoir. The red arrows indicate the flow path and direction of the medium; 'I' indicates sites where fluid was transferred by the automated liquid-handling instrument between the AV reservoir and input reservoirs of the channels of the different chips, as well as between the output and input reservoirs of different chips. **b**, Schematic of the MCRO in silico model of an individual organ chip. All organ chips have a similar barrier configuration that is composed of horizontally stacked compartments with volume (*V*), lower wall of the PDMS device (basal package (BP)), medium in the vascular channel (basal medium (BM)), endothelium (E), thin porous PDMS layer (membrane (M)), epithelium (H), medium in the parenchymal channel (apical medium (AM)), upper wall of the PDMS device (apical package (AP)) and the surface area normal to the cross-stream direction (S). All of the organ devices are represented by similar mathematical equations on the basis of drug mass balance in between the compartments, calculated for the drug flux *J* between the compartments (such as J_{AM-AP}) and the volumetric medium flow *Q* to give the drug concentration *C*. Each organ device was further discretized into three axial zones (proximal, central and distal), creating a 2D and less computationally demanding model to simulate a specific drug concentration over time. **c**, A schematic of the first-passage multi-organ-chip linked system, in which the organ-specific parenchymal epithelial cell layers of the gut, liver and kidney chips are represented by a drug-specific set of parameters for passive permeability, efflux and metabolism, determined experimentally in single organ-chip studies and then calibrated for the linked organ-chip system. The direction of flow (red arrows), drug package loss (dotted black arrows) and the percentage of input flow distributions from other organ chips versus the AV reservoir are also indicated in the diagram. Fig. 1 reproduced with permission from ref. [16], Springer Nature Limited.

represents the systemic circulation, and it can be used to measure blood and plasma concentrations of drug, which is critical for determining clinically relevant PK values. We modified the gut chip by lengthening its channels in a serpentine pattern (Fig. 1a) to increase the epithelial surface area by five times compared with the original design[15] and thereby enhance its absorptive capacity. Importantly, the presence of endothelium-lined vascular channels in all of the organ chips enabled the entire multi-organ system to be perfused with a common 'blood substitute' comprising an optimized endothelial cell medium containing a low level of serum[16] (see Methods). In this manner, fluid transfers between vascular channels of different organ chips both supports long-term viability and enables us to mimic physiological systemic drug transport between organs specifically through the endothelium-lined vasculature. The parenchymal channel of each organ chip is perfused with a different medium that is optimized for the organ-specific epithelium, providing another advantage over single-channel microfluidic devices. The ability to directly interface parenchymal and vascular tissues separated by a porous membrane in these two-channel organ chips is also crucial, as drugs normally pass across the endothelium–parenchymal

tissue interface of each organ in vivo, and the endothelium is a major contributor to drug toxicities as well as ADME and PK behaviours[18].

The common blood-substitute medium was transferred between the endothelium-lined channels of the different organ chips (that is, through input and output mini-reservoirs on each chip), and between the channels and the AV reservoir, using an automated organ-chip fluid-transfer instrument[16]. This instrument sequentially transfers multiple small volumes (as low as 0.05 ml) of medium between up to ten individual organ chips using a programmable robotic fluid handler (Fig. 1a, Supplementary Figs. 1 and 2) at given time points (from minutes to hours or days; Supplementary Table 3). This provides a major advantage over continuous (serial) fluid coupling because there is much less dead space, the system is fully reconfigurable and the same instrument can be used to automatically remove sample aliquots from the different fluid compartments for biochemical and mass spectrometry (MS) analysis. A detailed description of the chip handling, pipetting, perfusion and imaging capabilities of the instrument has been described previously[16], and additional details of timelines, experimental requirements and workload are provided in the 'Organ-chip linkage' section of the Methods. Incorporation of the AV reservoir into the system (Fig. 1a, Supplementary Figs. 1 and 2) also enables us to emulate drug dilution and systemic distribution due to blood flow through the entire human vasculature. This approach enabled us to normalize the total volume of the AV reservoir to the total human blood volume, and distribute flows from the AV reservoir to the vascular channel of each of the organ chips in a manner that corresponds to the percentage of cardiac output that flows to each of these organs in vivo (Supplementary Table 4). The AV reservoir also enabled us to overcome limitations of previous studies that used a simple serial linkage between different microfluidic multiphysiological systems[11,12,14]; these methods resulted in cumulative drug loss with each organ linkage due to the removal of experimental medium samples and replenishment with fresh medium. We observed the same limitation with serially linked two-channel organ chips (Supplementary Fig. 3). This setup also overcomes other limitations of serial organ-chip linking, including maintaining even flow and pressure throughout the system as well as physiologically relevant drug distributions and organ–organ interactions[12,16]. The greatest advantage, however, is that drug concentrations within the vascular channels of all of the chips can be measured using MS by sampling only the AV reservoir, and these quantitative values can then be compared directly to drug concentrations measured in blood samples from human clinical studies, thereby enabling IVIVT of PK parameters. As the automated system is used to transfer the blood-substitute medium from the AV reservoir in discrete time intervals every 12 h (twice each day) with each period of linking taking a maximum time of 40 min, this is to be taken into account in the experimental design, and it could pose a limitation for analysis of the PK/PD of drugs with short half-lives. To circumvent this limitation, we used computational PK/PD modelling to transform the discrete linking time points into continuous flow (Supplementary Fig. 1f,g, Supplementary Table 3) as described below.

A PBPK model for nicotine

To carry out quantitative IVIVT using this first-pass multi-organ-chip model, we developed a computational PBPK in silico model with biomimetic scaling on the basis of a validated PK/PD framework[18] using data generated by our experimental system. The workflow and rationale of our method are outlined in a three-step feedback loop (Supplementary Fig. 1f–h). Step one is to create initial in silico models using data obtained from experiments with individual organ chips in which small molecules or drugs (such as inulin or nicotine) were perfused through each device over 24–72 h. For example, a small molecular drug was infused into the lumen of the gut chip with or without living cells to mimic oral administration, and its concentrations in the apical and basal channel inlets and outlets were quantified using MS; similar studies were performed with the liver and kidney chips, but the drug was perfused through the vascular channels. These data were then used in combination with the physicochemical parameters of the drug and published values for active metabolism and transport functions of the various human organ-specific epithelium, as well as with results of quantifying passive drug absorption by the poly-dimethylsiloxane (PDMS) materials of the device and porous membrane (termed 'package loss' and measured without cells)[19], to develop computational models for each of the individual organ chips. These models were based on ordinary differential equation (ODE)-based, distributed (spatiotemporal), multi-compartment reduced-order (MCRO) models. The MCRO models were discretized in three axial zones (proximal, central and distal) along the flow axis to enable fast computation in linked organ-chip studies (Fig. 1b,c, Supplementary Figs. 1f,g and 4), which was validated against computationally demanding quasi-three-dimensional (3D) models. The MCRO model divides the organ chips into the following compartments: apical and basal medium channels, epithelial and endothelial cells, apical and basal PDMS package, and the PDMS membrane (Fig. 1c, Supplementary Fig. 4). A set of flux equations use various transport parameters and drug properties to calculate the drug transport across the barrier between compartments (equations (19)–(24); see Methods). These PK properties include passive permeability, efflux andmetabolism—which were measured for nicotine in each organ chip using MS—as well as their published physicochemical parameters, including unbound fraction, pH, pK_a (where pK_a indicates the negative log of the acid dissociation constant) and logP/logD (where logP and logD indicate the logs of partition and distribution coefficients, respectively, of a compound between oil and water phase) (Supplementary Fig. 4; see Methods). Compound losses were also incorporated into these model equations (equations (12)–(18); see Methods) using tracer and MS data. Assuming volumetric plug flow of medium through the channels, the solutions of the flux equations in between the compartments simulated specific drug concentrations over time, matching individual organ-chip output drug concentrations from the drug infusion experiments.

By creating a feedback design loop between experimental results generated in vitro with individual organ chips that were modelled computationally using our in silico system, and then integrating the individual models into a fluidically coupled first-pass computational model (Fig. 1c), we were able to develop, correlate, validate and optimize methods for determining drug metabolism pharmacokinetic (DMPK) parameters for the individual organ chips, as well as for the linked multi-organ-chip system. Computationally, the AV reservoir was integrated with the individual MCRO models for gut, kidney and liver chips (Fig. 1c, Supplementary Fig. 1f,g), and used to determine and implement optimal experimental linking parameters, such as dosing concentrations, timing of linking for drug infusion and wash-out, and volumes that would be required for the analysis (Supplementary Table 3). The in vitro linking experiment involved fluidically linking organ chips twice a day using the automated organ-chip instrument.

Under these conditions, all of the organ chips remained viable, as measured by low levels of lactate dehydrogenase release, and maintained stable human organ-specific functions, including an intestinal barrier with a low apparent permeability (P_{app}) in the gut chip, albumin production in the liver chip and proximal tubular reabsorption of albumin in the kidney chip during the 6 d of the study (Supplementary Fig. 5). Past studies that used the same organ chips individually (as opposed to fluidically linked) demonstrated physiologically relevant albumin reabsorption, alkaline phosphatase secretion and glucose transport[17] in the kidney chip; villus differentiation, mucus production, barrier function, increased CYP enzyme activity, and intestinal responses to radiation and microbiome in the

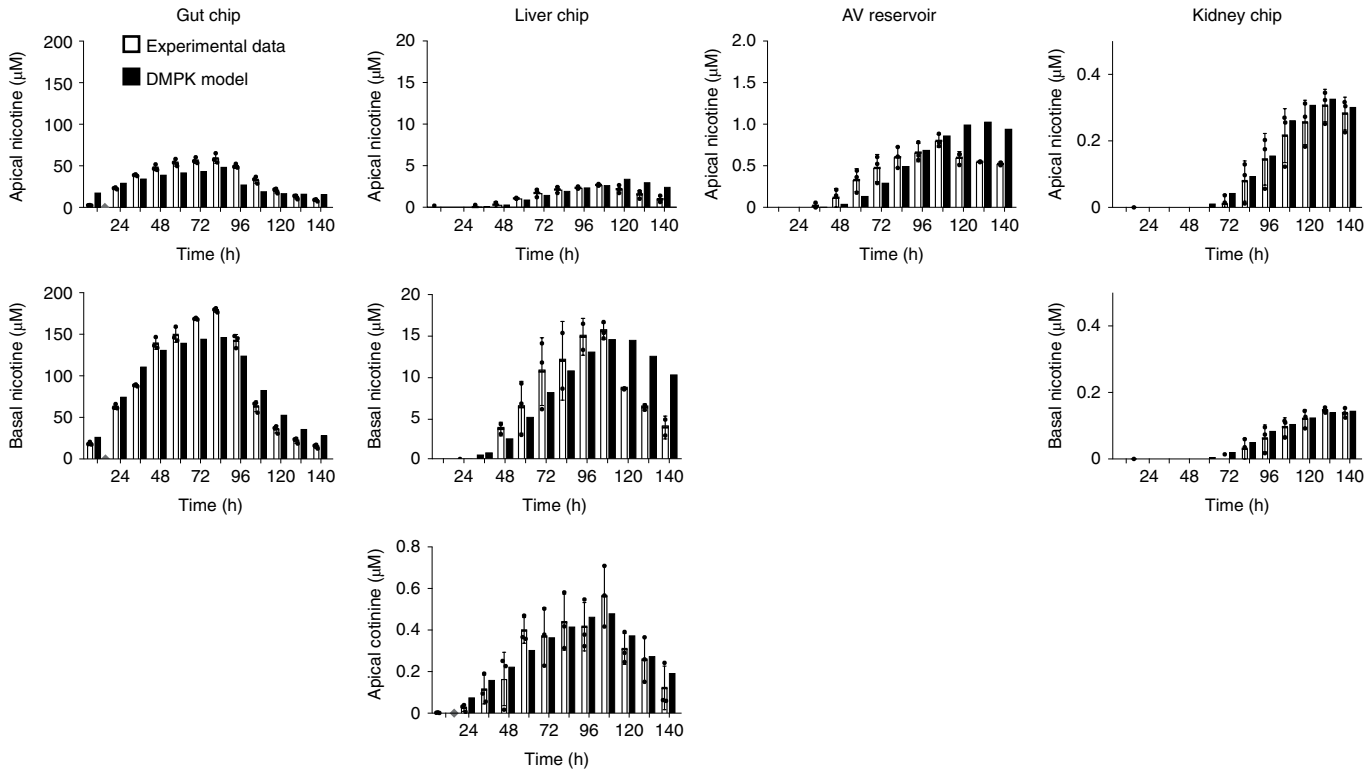

Fig. 2 | Mass spectrometry data and DMPK model of the first-pass multi-organ-chip system. Nicotine levels measured over time by MS within the apical and basal channels of the linked gut, liver and kidney chips, as well as in the AV reservoir, in cases in which nicotine was continuously infused through the lumen of the gut chip at a dose of 396 ± 16 μM for 84 h followed by a 56 h wash-out period (white bars) compared with predictions of the computational DMPK model (black bars). Values are also shown for the nicotine breakdown product, cotinine, in samples from the effluent of the epithelial channel of the liver chip. Data are mean ± s.d., pooled from three independent fluidically linked multi-organ-chip systems.

gut chip[15,20–22]; and maintenance of high clinically relevant levels of albumin production and multiple CYP-enzyme activities, as well as human-specific drug toxicities in the liver chip[23].

We then used this first-pass multi-organ-chip model to study the DMPK of the small molecule (161 Da) drug, nicotine. Nicotine is used as a drug to promote smoking cessation, and it is being explored as a potential therapy for neurodegenerative disease and ulcerative colitis[24], in addition to being the addictive component in tobacco products. Nicotine also has a low log[P], binds minimally to serum proteins and it is a well-studied tool compound. Moreover, clinical studies have shown that 20–45% of orally administered nicotine is bioavailable[25] and that it is metabolized by cytochrome P450 CYP2A6 in the liver, which is expressed by hepatocytes in our liver chips (Supplementary Fig. 5); the functionality of these chips have been extensively characterized previously[23]. As our kidney chip only recapitulates tubular functions[16,17], we compensated for the lack of glomerular function by distributing 40% of the input medium into the parenchymal channel of the kidney chip from the AV reservoir (Fig. 1a). This percentage was determined on the basis of previous clinical studies that revealed that 40% of the nicotine is unbound in vivo[25,26], as well as the known glomerular filtration rate for nicotine[27].

IVIVT of human PK parameters for nicotine

We then explored whether we could carry out IVIVT of nicotine PK using our MCRO-based DMPK modelling approach in combination with this fluidically coupled multi-organ-chip first-pass system by infusing a dose of nicotine (396 ± 16 μM as detected by MS) into the lumen of the gut chip to mimic oral administration for 84 h followed by a 56 h wash-out period (Fig. 1a,c, Supplementary Fig. 1, Supplementary Table 3). This oral dose was determined using the linked first-pass organ-chip MCRO models to ensure that both nicotine and its metabolite, cotinine, could be detected by MS in the vascular channels of all of the organ chips. On the basis of input from our model, combined with experimental constraints of medium loss due to sampling and evaporation, 90% of the input to the vascular channel of the gut chip was transferred from the AV reservoir, and the remaining 10% was fresh medium (Fig. 1c); inulin-FITC tracer also was included in the medium to confirm the accuracy of the robotic fluidic transfers. A portion (350 μl) of the gut chip's vascular outflow was then collected for sample MS analysis using the robotic sampler, and the remainder was transferred to the vascular channel of the liver chip, representing 23% of the total fluid input into this channel, with the remaining 77% coming from the AV reservoir (Fig. 1c). To include enterohepatic cycling that enables the recycling of small molecules in vivo, 350 μl of the vascular outflow from the liver chip was collected for sample analysis, and all of the remaining medium was transferred back into the AV reservoir, which then served as a source of part of the blood-substitute medium flowing into the vascular channel of the gut chip (Fig. 1c, Supplementary Table 3). The AV reservoir also provided 100% of the input into the vascular channel of the kidney chip, as well as 40% of the input into its parenchymal channel (with 60% being fresh organ-specific medium) to account for the absence of glomerular filtration. The parenchymal channels of all of the other organ chips were perfused individually with 100% organ-specific medium (Fig. 1c). The AV reservoir was replenished with fresh medium at every linking step to account for sampling and evaporative volume loss.

When we used MS to quantify nicotine in the AV reservoir and the effluents of the vascular channels of the different organ chips, the predictions of the computational DMPK model matched well with the experimental results over the full 140 h time course (Fig. 2,

Table 1 | Predictions of human PK parameters for oral nicotine obtained with two cohorts of multi-organ-chip IVIVT systems compared with clinical values and rodent clearance results

Nicotine PK parameters (systemic compartment)	Human (clinical data)[a]	In silico model (multi-organ chips)[d]
Nicotine gum (4.2 mg)		
C_{max} (μM)	0.052 ± 0.009	0.050 (δ = 3.8%, NS), 0.054 (δ = 3.8%, NS)
t_{max} (min) (range, minimum–maximum)	45 (19.8–90)	40.0 (δ = 11.1%), 38.9 (δ = 13.6%)
$t_{1/2(rise)}$ (min)[c]	10.60	20.45 (δ = 92.9%), 19.9 (δ = 87.7%)
$t_{1/2(fall)}$ (min)[c]	203	160 (δ = 21.1%), 263 (δ = 29.7%)
AUC (μM h)[b]	0.08 ± 0.02	0.062 (δ = 22.5%, P = 0.0007), 0.073 (δ = 8.75%, NS)
Pouched snus (14.7 mg)		
C_{max} (μM)	0.083 ± 0.032	0.101 (δ = 21.7%, NS), 0.088 (δ = 6.0%, NS)
t_{max} (min) (range, minimum–maximum)	60 (45–90)	66.7 (δ = 11.1%), 66.7 (δ = 11.1%)
$t_{1/2(rise)}$ (min)[c]	16.7	28.3 (δ = 69.6%), 31.7 (δ = 89.9%)
$t_{1/2(fall)}$ (min)[c]	152.6	236.6 (δ = 55.1%), 353.3 (δ = 131.5%)
AUC (μM h)[b]	0.13 ± 0.05	0.13 (δ = 1.5%, NS), 0.12 (δ = 9.2%, NS)
Loose snus (10.8 mg)		
C_{max} (μM)	0.064 ± 0.022	0.081 (δ = 26.5%, P = 0.003), 0.073 (δ = 14.1%, NS)
t_{max} (min) (range, minimum–maximum)	60 (45–90)	66.7 (δ = 11.1%), 66.7 (δ = 11.1%)
$t_{1/2(rise)}$ (min)[c]	13.7	28.3 (δ = 106.7%), 30.0 (δ = 119.0%)
$t_{1/2(fall)}$ (min)[c]	155.6	238.3 (δ = 53.2%), 353.3 (δ = 127.1%)
AUC (μM h)[b]	0.10 ± 0.03	0.106 (δ = 5.7%, NS), 0.098 (δ = 2.0%, NS)

C_{max} and AUC data are geometric mean ± s.d. [a]In vivo human clinical data from Digard et al.[28]. [b]AUC was computed for t = 0 to 2 h (that is, times when clinical measurements were available) for both in vivo and in silico studies. [c]Estimated using curve fitting for in vivo (on the basis of available clinical data); note that the estimated $t_{1/2(fall)}$ is beyond the measurement time window (curve-fit-based estimates may therefore not be reliable). [d]PK parameter values acquired with the two separate studies (δ is the percentage error between the clinical data and the model, followed by the one-sample t-test and Wilcoxon test for significance; NS, not significant).

Supplementary Fig. 1f,g). When we compared the DMPK models and the organ chips (including the AV reservoir) using Bland–Altman analysis, the bias in the models was less than 10% for all chips and the AV reservoir (Supplementary Fig. 7), resulting in good agreement between the model and experimental data. Further analysis revealed that all of the organ chips have good or very good scoring using Lin concordance coefficients. The liver chip exhibited the highest discrepancy between modelled and measured values (Pearson correlation r = 0.68; Supplementary Fig. 7), which was probably due to variation in metabolic activity that was not considered by the model. Furthermore, there was a high in vitro–in vivo correlation for nicotine bioavailability; the maximum level of nicotine that we measured in the AV reservoir (0.8 ± 0.08 μM; Fig. 2) was quantitatively similar to levels previously reported in humans (peak plasma concentrations of 0.05 to 0.6 μM)[27,28]. Furthermore, we detected production of cotinine (the hepatic breakdown product of nicotine) in the effluent from the apical hepatocyte channel of the liver chip, independently confirming that the liver chip expressed high levels of functional CYP2A6 activity, which is responsible for this conversion (Supplementary Fig. 5). Importantly, cotinine was also present at levels that correlated very well with the DMPK model (Lin's concordance coefficient = 0.82; Fig. 2, Supplementary Fig. 7). In these studies, CYP3A4 activity remained unchanged in the gut chip as did albumin production in the liver chip (Supplementary Fig. 6a), and we did not detect toxicity (lactate dehydrogenase release) in any of the first-pass human organ chips after nicotine exposure (Supplementary Fig. 6b), consistent with clinical findings[25]. Nicotine use has been shown to increase intestinal barrier function in humans[29], whereas this effect was not observed in non-smokers[30]. Similarly, we observed that administration of nicotine to the epithelial lumen of the gut chip significantly increased intestinal barrier function (P < 0.03) when we used the low-molecular-mass hydrophilic tracer Cascade Blue to measure permeability (Supplementary Fig. 8); however, we could not detect any effect using the less sensitive higher-molecular-mass inulin (Supplementary Fig. 6). We also did not detect a barrier change using trans-epithelial electrical resistance (TEER) measurements when the same intestinal epithelial cells and endothelial cells were interfaced across a porous membrane in a similar manner, but were cultured in static Transwell inserts (Supplementary Fig. 8). Although our findings are not consistent with a past study that reported that nicotine alters barrier function in Transwell cultures[31], a later study was unable to repeat the effect they observed[32].

To be relevant for pharmaceutical development, regulatory assessment and toxin testing, this fluidically coupled multi-organ-chip system must be able to carry out IVIVT and computationally predict drug DMPK parameters that are measured in humans in vivo in a quantitative manner. The geometric average of the maximum concentration (C_{max}) of nicotine that was measured in the blood of patients in a previous study using nicotine gum administered for 30 min orally was 0.052 ± 0.009 μM, with half the time to reach that level ($t_{1/2(rise)}$) of 10.6 min (Table 1). Although the human body has a closed continuous systemic circulation, these microengineered organ chips are discrete systems with extensive sampling requirements and experimental constraints; it is therefore difficult to recapitulate rapid changes in drug levels. Experimentally, this linked system also requires that flow is stopped periodically at discrete time points to collect experimental samples, replenish medium, visually inspect the tissues, and transfer fluids between the different organ chips and the AV reservoir.

To overcome this limitation of discrete fluid transfers and to predict clinically relevant blood nicotine concentrations, the second step in our workflow was to modify our validated DMPK model to computationally simulate continuous flow without fluid sampling on the basis of measurements obtained from the experimental system with discrete fluid transfers (Supplementary Fig. 1f,g). However,

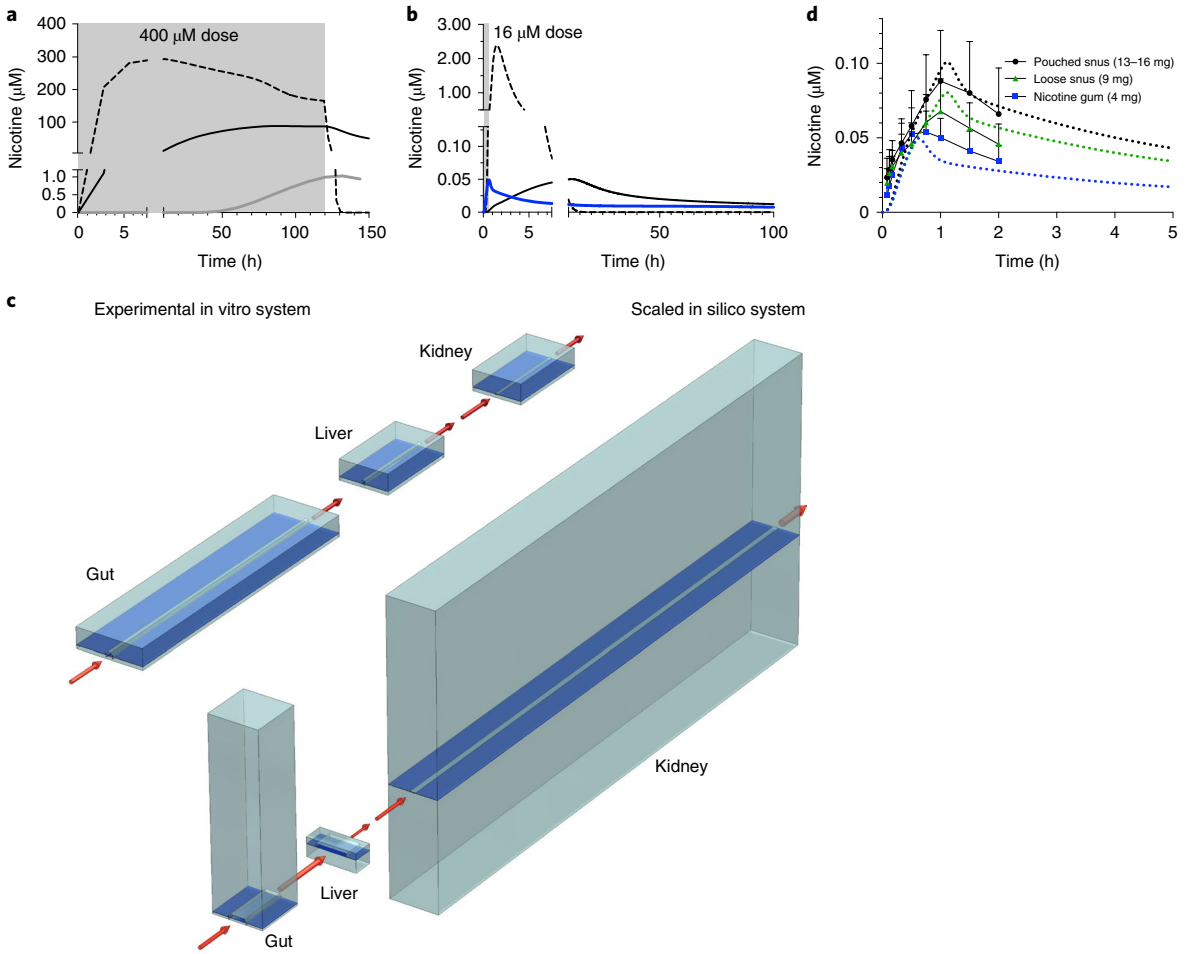

Fig. 3 | IVIVT of human PK parameters for nicotine using the multi-organ-chip first-pass system. a, The oral dose of nicotine (~400 μM) infused into the upper parenchymal channel of the gut chip (grey shaded area) and nicotine levels were measured in the AV reservoir over time in the real experimental system with discrete linkages every 12 h and package loss into the PDMS (grey solid line) versus computational DMPK model predictions of nicotine levels in which the same results were simulated as a continuous flow system with (black solid line) or without (dashed line) package loss. **b**, Predictions of nicotine levels in the AV reservoir using the same computational DMPK model as shown in **a**. A clinical nicotine dose of 16.15 μM and a 30 min infusion (grey shaded area) were simulated as a continuous flow system with (black solid line) or without (dashed line) package loss. The blue line shows that the in silico multi-organ-chip IVIVT system generated PK predictions for nicotine that much more closely matched the rapid PK dynamics of human blood nicotine values using a continuous flow simulation after it was optimized for physiological differences in cell mass and blood flow between the different organs in vivo, drug loss into the chip material and the geometry of endothelial channels to mimic drug transport. **c**, Comparison of the actual relative organ-chip channel volumes, flow rates and geometries shown in cross-section in the linked multi-organ system (top) and the scaled values for these properties used for the IVIVT simulations (bottom). **d**, Changes in nicotine blood concentrations over time predicted by the optimized scaled in silico multi-organ-chip IVIVT system for three different oral doses (different coloured dashed lines) closely match previously published blood nicotine levels that were measured in patients who received orally administered nicotine in the form of nicotine gum (blue; the same curve as the blue curve in **b** shown at different scale), pouched snus (black) or loose snus (green) at three different doses (4 mg, 9 mg and 13–16 mg, respectively)[28]. Similar results were obtained in two separate studies, each with three independent fluidically linked multi-organ-chip systems.

this continuous model did not produce a clinically relevant C_{max} value for nicotine when using the high dose of 396 ± 16 μM, as suggested by the MCRO model, even when the experimentally determined package loss of nicotine into the PDMS was integrated into the model (Fig. 3a). We then used the optimized DMPK model that simulates continuous linking in the organ chips and AV reservoir on the basis of experimental discrete sampling measurements and input dose concentration and timing parameters from a previously published clinical study in patients who were given chewable nicotine gum[28] (oral dose of 16 μM nicotine for 30 min). Notably, the initial prediction of this continuous DMPK model on the basis of our experimental data incorporating the optimized package loss into the PDMS materials estimated a C_{max} of 0.055 μM, which is in the 95% clinical confidence interval; however, the model predicted a $t_{1/2(rise)}$ of 16 h, which is considerably different to the 10.6 min that was observed in vivo (Fig. 3b).

To further enhance the accuracy of performing IVIVT of these clinical DMPK parameters, we undertook a third step in our workflow and implemented a scaling approach in the MCRO model on the basis of intrinsic PK parameters (such as intrinsic clearance)[33] (see Methods), which effectively changes the biomass and also accounts for PDMS adsorption in the various organ chips, with the goal of optimizing the ability of the model to predict the human nicotine C_{max} and $t_{1/2(rise)}$ previously reported in vivo[28]. This was possible because, using this scaled IVIVT model, we were able to extend our in vitro DMPK studies into experimentally intractable regimes

Table 2 | Predictions of human PK parameters for intravenous cisplatin obtained with the multi-organ-chip IVIVT system compared with clinical values

Cisplatin PK parameters (systemic compartment)	Human (clinical data)[a]	In silico model (multi-organ chips)[c]
Cisplatin (1 h infusion)		
C_{max} (μM)	18.02 ± 4.93	22.72 (δ = 26.1%, P = 0.0146)
t_{max} (h)	~1.0	1.0
AUC (μM h)[b]	41.94 ± 12.41	48.27 (δ = 15.1%, NS)
Cisplatin (3 h infusion)		
C_{max} (μM)	30.30 ± 6.48	37.26 (δ = 23.0%, P = 0.0079)
t_{max} (h)	~3.0	3.0
AUC (μM h)[b]	253.33 ± 100.32	252.6 (δ = 0.4%, NS)

C_{max} and AUC data are geometric mean ± s.d. [a]In vivo human clinical data Rajkumar et al.[38]. [b]AUC was computed for times when clinical measurements were available for both in vivo and in silico studies. [c]δ is the percentage error between the clinical data and the model, followed by the one-sample *t*-test and Wilcoxon test for significance.

and computationally redesign the geometry of the organ chips, and create designs that are difficult or impossible to fabricate or implement experimentally. The optimal, scaled first-pass modelling system included physiologically relevant changes, including increased biomass in the in silico version of the liver chip, a larger surface area in the kidney chip and decreased absorptive surface area in the gut chip (Fig. 3c, Supplementary Fig. 1,h). Moreover, all vascular channel geometries were computationally changed to include dimensions with a smaller height and larger width (Supplementary Table 5), effectively creating shorter diffusion distances in the vascular compartment. In the human body, there is also often substantial drug loss into peripheral tissues, such as fat; therefore, to incorporate this feature of drug behaviour into the model, we also systematically varied our package loss parameter from 0% to 100% (Supplementary Fig. 9, Supplementary Table 5). The highest correlation with clinical nicotine data corresponded with a package loss of 34% in our model (Supplementary Table 5). Moreover, we integrated specific human in vivo anatomical parameters into the in silico continuous first-pass model, including organ-specific fractional blood flows, blood flow rates and dimensions of the major vessels (Supplementary Table 4), which were used to computationally scale the volumes and flow rates of the vascular channels, and the dimensions of tubing that connect fluid input and output reservoirs to each respective organ chip.

Importantly, when this optimized scaled in silico IVIVT model was applied to our in vitro experimental data for oral administration of nicotine through the first-pass, multi-organ-chip system and was used to simulate changes in nicotine levels in the AV reservoir as a correlate for systemic blood levels, the IVIVT model quantitatively predicted a drug exposure profile and time course that closely mimicked the profile observed in vivo in patients after equivalent dosing with nicotine gum (Fig. 3d, Supplementary Fig. 10). We have thereby demonstrated how we can use multi-organ-chip system experimental data generated over 140 h to create an IVIVT model that can predict drug PK over 30 mins in patients[28]. This optimized model accurately predicted an effective nicotine concentration in the AV reservoir (0.055 μM) that is in the 95% confidence interval of the clinical C_{max} (0.052 ± 0.009 μM) that was previously measured in patients[28]. The PK profile predictions from two datasets of experiments in which nicotine was tested in the multi-organ-chip setups (Tables 1 and 3) also matched the clinical data, predicting the time required to reach the maximum levels (t_{max}) of 38.9 min, in the clinical range of 18.9–90 min (ref. [28]). Furthermore, when we compared predictions of the scaled in silico in vitro-to-in vivo extrapolation (IVIVE) model for two different nicotine-containing tobacco formulations (pouched snus and loose snus; two forms of oral administrated tobacco), dosing times and doses, we again observed a close match (Tables 1 and 3) between the predictions of the model and the clinical drug dose time courses, even though our model was developed using a different drug dose and formulation (Fig. 3d, Supplementary Figs. 7 and 10, Supplementary Table 6). The predicted C_{max} values deviated at most by 26.5% from the clinical value for pouched snus; by contrast, for other formulations, the discrepancy was not significant. Predicted t_{max} were all within clinically measured range, and the area-under-curve (AUC) value deviated at most by 22% from the predicted value (Tables 1 and 3, Fig. 3d). The Bland–Altman analysis and Pearson correlations revealed that the bias of the model predictions was at most 16% of the C_{max} values and Lin's concordance coefficients were all rated good to very good (Supplementary Fig. 7). Furthermore, when we compared our IVIVT results with data using organ-specific PK parameters from rodents[34], the human multi-organ-chip system better predicted the clinical liver intrinsic clearance results than the rat (Tables 1 and 3). Importantly, although secondary intrinsic liver clearance cannot be observed in rodents, we can derive this kinetic parameter from the AV reservoir concentration curve. However, for renal clearance, the rodent model predictions were closer to the clinical data; this is probably because we lack a glomerulus in the kidney chip model and instead used simulations to computationally compensate for the urinary clearance.

Prediction of human PK/PD parameters for cisplatin

To explore whether this computational IVIVT approach using the multi-organ-chip system might have broader applicability, we applied the PBPK model developed for nicotine to predict human PK parameters for a second drug—the cancer chemotherapeutic cisplatin—using a different path of administration. Cisplatin is administered intravenously in patients and inhibits cancer cell growth by interfering with DNA synthesis and repair[35], leading to a wide range of adverse effects, including myeloid toxicity in bone marrow and renal toxicity[35]. Therefore, by modifying the multi-organ-chip system by administering 160 μM cisplatin directly into the AV reservoir to mimic intravenous injection and replacing the gut chip with a human bone marrow chip (Fig. 4a, Supplementary Figs. 2e and 11a, Supplementary Table 3) that reconstitutes myeloid and erythroid cell production in vitro and recapitulates drug-induced bone marrow drug and radiation toxicities[36] (Supplementary Fig. 11b), we were able to analyse drug PD as well as carry out PK modelling. To do this, we followed our workflow for IVIVT multi-organ-chip models. First, a MCRO DMPK model of the bone marrow chip was developed on the basis of single-chip data (Supplementary Fig. 11c), and then it was integrated with the liver chip, kidney chip and AV reservoir in silico models developed for the nicotine study (Fig. 4a). Experimentally, the lack of glomerular function was compensated

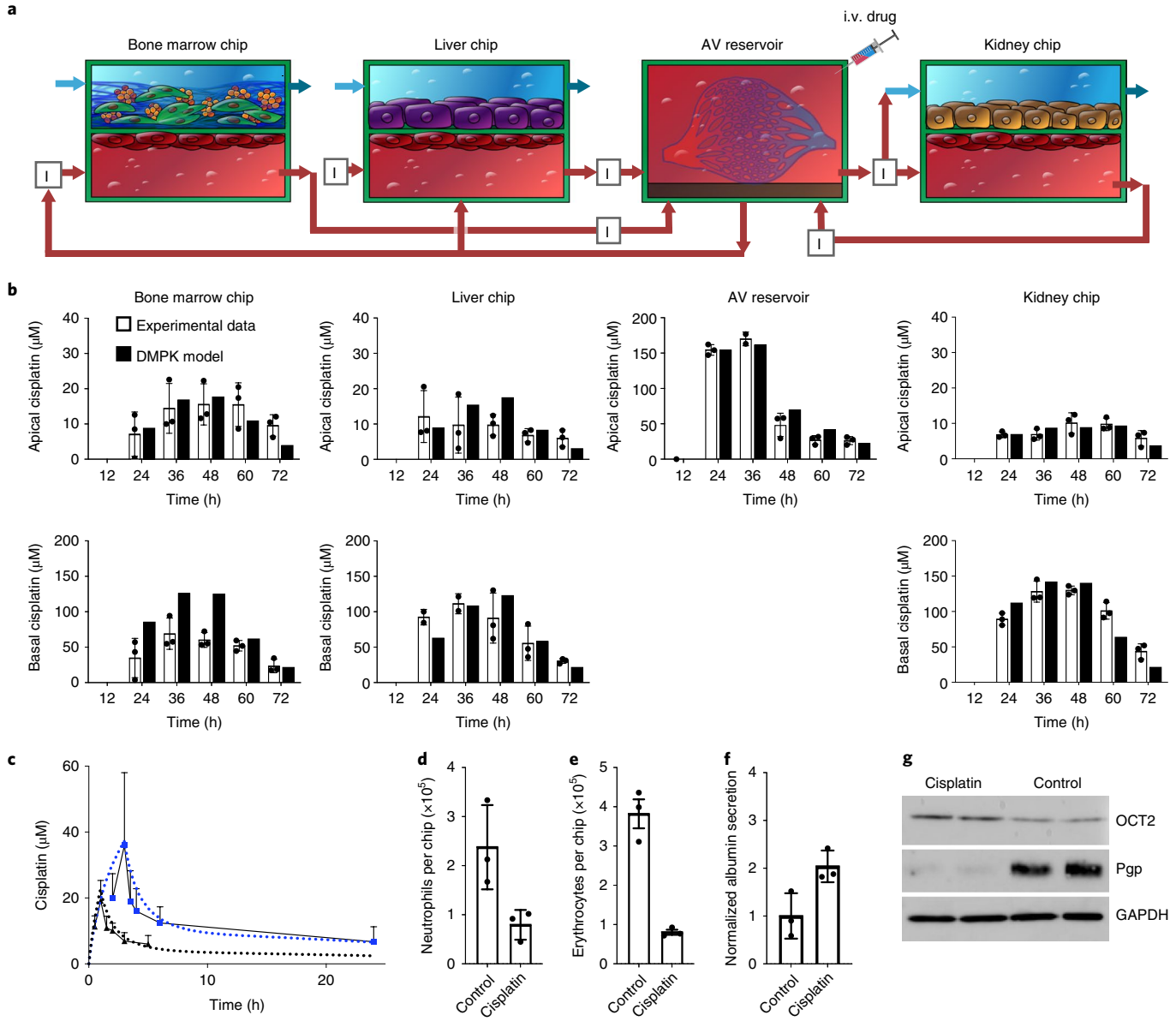

Fig. 4 | Prediction of cisplatin PK and PD parameters using the multi-organ-chip IVIVT system. a, The fluidic coupling path of the bone marrow, liver and kidney chips linked to the AV reservoir in the multi-organ-chip system was used to study cisplatin PK. The red arrows indicate medium flow path and direction. Cisplatin (160 μM) was continuously infused into the AV reservoir for 24 h to simulate intravenous (i.v.) infusion followed by a wash-out period of 48 h. **b**, Cisplatin concentrations measured over time in medium samples collected from the effluent of each chip and the AV reservoir using MS (white bars) compared with predictions of the optimized scaled DMPK model (black bars). Data are mean ± s.d. **c**, Changes in cisplatin concentrations in blood over time predicted by the optimized scaled multi-organ-chip IVIVT system for infusion periods (dotted lines) of either 1 h (black) or 3 h (blue) closely match previously published measurements of blood cisplatin levels measured in patients who received cisplatin injected intravenously over these times[38] (solid lines). Similar results were obtained in three replicate experiments. **d**–**g**, Cisplatin infusion in the multi-organ-chip system (three independent fluidically linked multi-organ-chip systems) resulted in the suppression of total of neutrophil (**d**) and erythroid (**e**) cell numbers in the bone marrow chip, as determined by FACS analysis (for **d**, centre value control, 2.38×10^5 neutrophils per chip; cisplatin, 0.79×10^5 neutrophils per chip; for **e**, control, 3.82×10^5 erythrocytes per chip; cisplatin, 0.81×10^5 erythrocytes per chip). Albumin production was not significantly decreased in the liver chip (**f**), shown as albumin secretion normalized to control chips (centre value control, 1; cisplatin, 2.04), therefore recapitulating cisplatin PD in vitro. For **c**–**f**, data are mean ± s.d. **g**, Western blot analysis also revealed that cisplatin increased OCT2 and decreased Pgp levels in kidney chips compared with controls; similar results were obtained in two different experiments. GAPDH is shown as a loading control.

for by transferring 5% and 95% of the AV reservoir medium to the apical parenchymal and basal vascular channels of the kidney chip, respectively (Fig. 4a), on the basis of the ~5% unbound fraction of cisplatin in vivo[37]. We then monitored drug metabolism and clearance by the liver and kidney chips, as well as toxicity in the bone marrow chip, when cisplatin was introduced into the AV reservoir to mimic intravenous injection. Again, we obtained a good correlation between the predictions of the DMPK model and experimental cisplatin levels measured in the effluents of each chip and the AV reservoir[38] (Fig. 4b, Tables 2 and 3, Supplementary Figs. 12 and 13). As in the case of nicotine, the Bland–Altman analysis revealed that errors in the DMPK models do not correlate with cisplatin

Table 3 | Predictions of human PK parameters for oral nicotine and intravenous cisplatin obtained with the multi-organ-chip IVIVT system compared with clinical values and rodent clearance results

	PK parameters	Rodent (in vivo)[a]	Human (clinical data)[b]	In silico model (multi-organ chips)[c]
Nicotine				
Gut	P_{app} (10^{-6} m s^{-1})	NA	9.5–57.2	1.3–7.5 (δ = 21–98%)
Liver	CL_{int} (ml min^{-1} kg^{-1} of bodyweight)	300	12.5	10.0 (δ = 20%) 8.004 (δ = 36.0%)
	$CL_{int,sec}$ (ml min^{-1} kg^{-1} of bodyweight)	NA	0.74	0.15 (δ = 80.0%)
Kidney	CL_R (ml min^{-1} kg^{-1} of bodyweight)	5.5	0.5–1.29	0.03–0.13 (δ = 75–98%)[a]
Cisplatin				
Clinical data	In silico model (multi-organ chips)			
Liver	CL_{int} (ml min^{-1} kg^{-1} of bodyweight)	3.73	0.25	0.20 (δ = 20.0%)
Kidney	CL_R (ml min^{-1} kg^{-1} of bodyweight)	0.19	1.39	0.008 (δ = 99.4%)

CL_{int}, intrinsic clearance; $CL_{int,sec}$, secondary intrinsic clearance; CL_R, renal clearance. NA, not available. [a]Rodent in vivo data for nicotine from Yamazaki et al.[34] and for cisplatin from Gong et al.[68], in which total cisplatin clearance was used for liver clearance and clearance out of kidney tissue. [b]Human in vivo data for nicotine from Digard et al.[28] and for cisplatin from Rajkumar et al.[38], in which total cisplatin clearance was used for liver clearance and clearance out of kidney tissue. [c]δ is the percentage error between the clinical data and the model; two values are indicated when two separate studies resulted in different values.

concentration. In all cases except for the bone marrow chip basal data, the bias value did not exceed 11% of the maximum observed concentration in each chip (Supplementary Fig. 12). The Lin concordance and Pearson correlation analyses also demonstrated that the model predicted cisplatin levels in the AV reservoir with high accuracy ($\rho = 0.98$ and $r = 0.99$, respectively); however, the liver and bone marrow apical channels were only moderately well captured by the DMPK model ($\rho = 0.53$ and 0.53, $r = 0.76$ and 0.86, respectively; Supplementary Fig. 12).

In the cisplatin IVIVT analysis, we retained the same scaling parameters for organ chips, package loss and tubing that were used in the nicotine study except that for this setup, the gut chip was replaced by the bone marrow chip (Fig. 4a), again using appropriate in vivo anatomic parameters (Supplementary Table 6) to scale organ-chip dimensions and flows (Supplementary Table 7). The only change was that the medium volume in the AV reservoir was decreased to account for the relative change attributed to the smaller volume of the major vessels in the bone marrow compared with the intestine in humans, as well as changes in geometry between the two chips and the mode of administration[39,40] (see Methods; Supplementary Tables 6 and 7). Importantly, our optimization showed that reducing the percentage of the AV reservoir volume from 93.83% (~7 ml) for nicotine to 30.23% (~2.5 ml) for cisplatin resulted in better correlation (Supplementary Figs. 12 and 13) between the computational IVIVT predictions of the model using a cisplatin dose of 160 ± 11 µM administered through the AV reservoir and the vascular channels of the linked organ chips, including the bone marrow chip for 24 h. The results were compared to a previously published clinical study in which cisplatin was administered intravenously to patients at different doses and for different durations (18 ± 5 µM or 30 ± 6 µM for 1 h or 3 h, respectively; Fig. 4c, Tables 2 and 3). Specifically, there was no significant difference between the AUC_{1h} ($P = 0.1412$, one-sample t-test) and the AUC_{3h} ($P = 0.9738$, one-sample t-test), whereas there was 26% and 23% discrepancy ($P = 0.015$ and 0.008, respectively) between the clinical C_{max} and the modelled data (Tables 2 and 3). However, Bland–Altman plots demonstrated that the bias was only around 13% of the maximum drug concentration and the Lin's concordance and Pearson coefficients showed good to very good correlation (Supplementary Fig. 13). Furthermore, when we compared the IVIVT predictions with rodent data, the linked human organ-chip system again provided better estimations of intrinsic liver clearance than renal clearance, possibly due to the fact that we estimated glomerular function and the drug is highly bound to albumin[41] (Tables 2 and 3). Importantly, these data show that in silico multi-organ-chip models with the same scaling can be applied to predict clinical PK profiles of two different drugs, each with a distinct dosing regimen, route of administration (oral and intravenous) and mechanism of toxicity.

It is important to note that we did not analyse the specific influence of fluid transfers on organ-chip function because this is the focus of a separate study in which eight organ chips (including gut, liver, kidney and bone marrow chips) were linked for 3 weeks of culture using the same automated culture instrument[16]. However, the levels of albumin reabsorption in the kidney chip, intestinal barrier function in the gut chip and production of neutrophils and erythrocytes in the bone marrow chip in this study are similar to or better than those measured in the eight-chip linking study. For example, albumin production in the liver chip measured here was similar to that in the stand-alone liver chip, and these levels were higher than the levels detected when it was linked to seven other organ chips, demonstrating that chip linkage procedures can influence organ metrics. More importantly, our finding that we can quantitatively predict human clinical PK for two different drugs using two different administration routes indicates that the organ chips functioned in a physiologically relevant way when fluidically linked in this study.

Finally, we used the fluidically coupled multi-organ-chip model to carry out human PD analysis in vitro. When cisplatin was flowed through the vascular channel of the linked organ chips at the same dose for 24 h, we detected myeloid toxicity as indicated by a 78% reduction in the total number of cells in the bone marrow chip ($P = 0.001$; Supplementary Fig. 14a). Additional fluorescence-activated cell sorting (FACS) analysis revealed 67% and 72% reductions in neutrophils (Fig. 4d; $P = 0.0396$) and erythrocytes (Fig. 4e; $P = 0.0013$), respectively, therefore recapitulating the known side effects of cisplatin in patients (neutropenia and anaemia, respectively) in vitro[35]. Cisplatin does not produce hepatotoxicity at clinically relevant doses in patients, and we similarly could not detect a decrease in albumin production (Fig. 4f) or CYP3A4 function (Supplementary Fig. 14b) in the liver chip. By contrast, cisplatin exposure resulted in a reduction in P-glycoprotein (Pgp) expression and upregulation of OCT2 in the kidney chip (Fig. 4g), which are membrane transporters that have been shown to be affected by cisplatin-mediated toxicity[42]. Interestingly, although the same patterns of upregulation of OCT2 and downregulation of Pgp have been observed in rat kidney slices that were exposed to cisplatin at doses similar to what we applied in the kidney chip, longer-term

in vivo rat studies have shown the reverse pattern[42,43]. This discrepancy could be due to the fact that we used a lower dose and shorter time duration of cisplatin in our study. Alternatively, our human multi-organ-chip model might more effectively recapitulate early cisplatin PD in the human kidney than rats.

Discussion

Taken together, these findings demonstrate that this fluidically coupled, multi-organ-chip-based, IVIVT system can be used to predict quantitative human PK parameters in vitro that are highly similar to those obtained in human clinical studies. We performed IVIVT using an in silico DMPK model built using experimental data obtained from multiple two-channel human organ chips that were fluidically coupled by transferring a universal blood substitute between endothelium-lined vascular channels and incorporating an AV reservoir to mimic drug distribution and dilution through the entire vasculature. This is in contrast to previous studies that either only computationally simulated IVIVT using theoretical models of fluidically linked microfluidic culture systems without experimental validation[12,14] or applied PK/PD models using linked cell-containing microfluidic devices that lacked physiologically relevant endothelial barriers[44]. We have previously shown that the endothelium is vital to recapitulate many in vivo physiological functions, including liver chip metabolic function[16]. As a result of the more faithful physiological mimicry included here, and the use of more advanced MCRO-based DMPK models, we were able to model drug transport across the endothelial–parenchymal tissue barrier and develop an IVIVT approach that provides an excellent quantitative fit between predictions of human PK on the basis of in vitro studies and data from clinical studies. It should be noted that some previous models have been able to predict C_{max} for drugs in humans, but they did not predict relevant drug residence times[40] as we did here. In our studies with cisplatin, we were also able to recapitulate organ toxicities of this drug that are observed in humans, as well as the lack of hepatotoxicity. These data, combined with the altered gut chip barrier function and kidney transporter changes after nicotine exposure, further demonstrate the biological relevance of this model. Together these data suggest that this IVIVT modelling system may be useful for studying—and potentially predicting—drug PD.

This first-pass multi-organ-chip model does not include other important human organs that can influence drug PK, including drug absorbing fat tissues. However, we are able to compensate for this limitation using in silico modelling that can create virtual drug absorbing tissues, for example, by modulating the absorptive properties of the chip PDMS materials in our package-loss estimations, and by changing the organ-chip dimensions to best predict in vivo-like drug uptake. Drug absorption and package loss were optimized to the same level to faithfully recapitulate both nicotine and cisplatin PK in this study; however, for drugs with different properties and hepatic clearance rates, the PDMS absorption needs further optimization. The computational model was also used to compensate for the absence of glomerular function that normally contributes substantially to urinary clearance, and to circumvent potential limitations due to the absorption of drugs into the PDMS device materials. In this manner, this human-relevant fluidically coupled multi-organ-chip PK/PD modelling system enables users to perform IVIVT to quantitatively predict human PK parameters in vitro (the full procedure, from initial drug selection to IVIVE, is outlined in Supplementary Fig. 15). Thus, the multi-organ-chip PK/PD modelling system may provide an experimentally tractable human system for drug discovery, regulatory assessment, toxicological evaluation and personalized medicine (using patient-specific cells) in addition to accelerating therapeutic development by enabling more effective design of drug regimens for future phase-I clinical trials.

Methods

Organ-chip fabrication. The gut, liver and bone marrow chips, which contain a central porous (7 μm diameter) membrane separating two linear parallel channels, were fabricated from PDMS using a previously published soft lithography method[45]; a description of channel dimensions and membrane features is provided in Supplementary Table 1. The kidney chips were fabricated from PDMS upper and lower walls containing formed microchannels (0.1 mm height × 0.1 mm width × 24 mm length) with a polyester terephthalate track-etched membrane (0.4 μm pores) sandwiched in between and bonded, as previously described[46]. The gut chip was fabricated containing a serpentine channel (Fig. 1a) to increase absorptive area; it was mechanically actuated to mimic peristalsis-like motions using a programmable vacuum regulator system that was built in-house that applies cyclic suction to hollow side chambers that run on either side of the central culture channels, thereby rhythmically deforming the porous membrane and attached cells, as previously described[15]. The bone marrow chip used in this study had oval-shaped upper and lower chambers composed of PDMS (Supplementary Figs. 2 and 11), and the upper chamber had an open top that was closed with a resealable medical-grade adhesive film (Adhesives Research) to enable loading of the matrix gel laden with cells.

Microfluidic organ-chip culture. Our methods for plating and culture of parenchymal and endothelial cells within the gut, liver, kidney and bone marrow chips were described previously[15–17,23,36]. We used the gut chip lined with Caco-2 intestinal epithelial cells to minimize cell source variability and ensure the robustness of this initial proof-of-principle IVIVT study, as we have previously shown that—when cultured in the presence of physiologically relevant luminal flow and peristalsis-like mechanical deformations—these chips display formation of intestinal villi lined by all four epithelial cell lineages of the small intestine and have enhanced barrier function, drug-metabolizing cytochrome P450 activity and apical mucus accumulation compared with the same cells grown in conventional Transwell cultures[15,22]. However, this cell line could be replaced in the future with primary intestinal epithelial cells derived from organoids isolated from patients as recently described[21]. A detailed description of the design, capabilities and control systems of the automated multi-organ-chip culture system for transferring medium samples between chips, as well as for analysis, has also been described previously[16]. Our methods for coating the chips and plating cells in the gut, liver, kidney and bone marrow chips used in the present study are provided in Supplementary Table 2. In brief, to create a human gut chip, the PDMS chip was pre-coated with Matrigel (1%, Corning) and Collagen type I (100 μg ml^{-1}, Corning) before Caco-2 BBe cells (acquired from the Harvard Digestive Disease Center) were plated (1.5×10^5 cells per cm^2) in the upper channel, and human umbilical cord vascular endothelial cells (HUVECs, Lonza) were seeded (1.5×10^5 cells per cm^2) on the opposite side of the porous membrane in the lower channel. The upper parenchymal channel was perfused (60 μl h^{-1}) with DMEM-High Glucose (Gibco, Thermo Fisher Scientific) supplemented with 10% heat-inactivated FBS (Gibco, Thermo Fisher Scientific) and 1% penicillin–streptomycin (Gibco, Thermo Fisher Scientific). We used a common universal blood-substitute endothelial medium to perfuse (60 μl h) the vascular channel of the gut chip, as well as all other organ chips and the AV reservoir, that is composed of DMEM/F12 (Gibco, Thermo Fisher Scientific) with EGM-2 supplements and growth factors (Lonza), 1% penicillin–streptomycin (Gibco, Thermo Fisher Scientific) and 0.5% FBS (Gibco, Thermo Fisher Scientific). After culture for 1 d, cyclic suction was applied to side chambers to recreate peristalsis-like deformations on-chip (10% strain, 1.2 Hz), which were maintained throughout the course of the experiment.

In the liver chip, human primary liver sinusoidal microvascular endothelial cells (Cell Systems) were first plated (1×10^5 per cm^2) for 1 h on the lower surface of the porous PDMS membrane in the lower channel of PDMS chips that were precoated with collagen I (300 μg cm^{-2}, Corning). The chips were then turned upside down and human primary hepatocytes (Thermo Fisher Scientific) were seeded (2.5×10^5 cells per cm^2) in the upper channel. After 3 h, the hepatocytes were overlaid with Matrigel (250 μg ml^{-1}, Corning) in hepatocyte maintenance medium (Thermo Fisher Scientific). Then, 1 d later, the Matrigel-containing medium was changed to fresh hepatocyte maintenance medium, which was then perfused (60 μl h^{-1}) through the upper channel for the rest of the experiment, while the blood-substitute medium was perfused at the same rate through the lower channel. The liver sinusoidal endothelial cells contribute substantially to the function of the chip, for example, liver chips with liver sinusoidal endothelial cells exhibit around 3× higher CYP3A4 metabolic activity than those without[16].

In the kidney chip, primary human glomerular microvascular endothelial cells, GMVECs (Cell Systems, ABRI128), were first plated (1×10^5 cells per cm^2) for 1.5 h in the lower channel of chips containing PTE membranes that were precoated with collagen IV (500 ng cm^{-2}, Sigma-Aldrich) and laminin (500 ng cm^{-2}, Sigma-Aldrich). The chips were then inverted and primary human renal proximal tubule epithelial cells (ScienCell Research Laboratories, 4100, donor lot 5110), were plated (1.2×10^5 cells per cm^2) in the upper channel. After being allowed to attach for 2 h, the cells were perfused (60 μl h^{-1}) with DMEM/F12 (Gibco, Thermo Fisher Scientific) supplemented with 10 ng ml^{-1} EGF (Thermo Fisher Scientific), 440 μg ml^{-1} adrenaline (Sigma-Aldrich), 36.25 μg ml^{-1} hydrocortisone (Sigma-Aldrich), 67.3 μg ml^{-1} triiodothyronine (Sigma-Aldrich), 5 μg ml^{-1} insulin

(BioVision), 5 μg ml^{-1} transferrin (Sigma-Aldrich), 1% penicillin–streptomycin (Gibco, Thermo Fisher Scientific) and 0.5% FBS (Lonza). The universal endothelium medium was again perfused at the same rate through the vascular channel.

In the bone marrow chip, HUVECs were first plated (1×10^5 cells per cm^2) on the lower surface of the porous membrane in the lower channel of PDMS chips that were precoated with fibronectin (100 μg ml^{-1}, Gibco) and collagen I (50 μg ml^{-1}, Gibco). Then, 1 h later, 1×10^4 primary human CD34$^+$ progenitor cells were added to StemSpan SFEM II basal medium (STEMCELL Technologies) supplemented with Collagen I (0.2 mg ml^{-1}, Sigma-Aldrich) and thrombin (0.5 U ml^{-1}, Sigma-Aldrich), and then 37 μl of this solution was combined with 14 μl of a solution containing fibrinogen (5 mg ml^{-1}, Sigma-Aldrich) and aprotinin (0.025 mg ml^{-1}, Sigma-Aldrich). The total solution (50 μl) was introduced into the open apical channel of each chip and allowed to solidify at room temperature for 10 min; the upper channel was then sealed with clear medical-grade adhesive film. The upper channel of the chips was perfused (at 67 μl min^{-1} with StemSpan SFEM II medium supplemented with 10% FBS, 1% penicillin–streptomycin (12.5 μg ml^{-1}), aprotinin (25 ug ml^{-1}, Sigma-Aldrich), erythropoietin (20 ng ml^{-1}, PeproTech), G-CSF (1 ng ml^{-1}, PeproTech), Flt3-L (100 ng ml^{-1}, PeproTech), TPO (100 ng ml^{-1}, PeproTech) and SCF (50 ng ml^{-1}, PeproTech). The CD34$^+$ cells and stromal cells were isolated from whole blood and apheresis samples from normal human donors undergoing peripheral blood mobilization at the Massachusetts General Hospital. The cells were purified using CD34$^+$ microbeads (Miltenyi) and frozen in RPMI (Thermo Fisher Scientific) with 10% FBS and 10% DMSO (EMD Millipore). Transwells (24-well plate, Corning, 0.4 μm pore size, polyester terephthalate membrane) were coated on both sides with coating solution as described for the gut chip. Caco-2 BBe cells and HUVECS were seeded on either side of the membrane at 100,000 cells per cm^2. Transwells were kept with apical and basal medium, as described for the gut chip, which was changed every 2–3 d for 4 weeks and then assayed.

Organ-chip linkage. The organ chips were linked using an automated liquid-handling instrument. A detailed description of the system is reported in the companion paper[16]. In summary, an automated liquid-handling instrument, which can hold and link up to ten organ chips and an AV reservoir, was custom built so that it can fit inside a standard incubator. Before linking the organ chips, each organ was placed in quarantine and then perfused without linking for 24–48 h to ensure that the chips were in their optimal condition. After all of the organ chips were placed onto the instrument, the linkage protocol was performed as described in Supplementary Table 3. Levels of flow-induced shear stress within all of the organ chips were in the same range as previously reported[17,22].

A multi-organ-chip study can take 2–3 weeks to carry out (Supplementary Table 8) in cases in which validated cells are used, chips are seeded and matured individually and appropriate assay procedures are developed; this duration is similar to the length of traditional preclinical evaluation studies in animals. Technically, organ-chip handling, system setup analysis and IVIVT are different compared with classical preclinical models and, therefore, an additional training period (of around 2–4 weeks) is required as well. Although the use of a larger number of different organs chips demands several skilled technicians, the four organ chips that we used in this study are manageable with two trained staff members.

Analytical methods. To determine barrier function in the gut chip, the inert tracers inulin-FITC (Sigma-Aldrich) or Cascade Blue hydrazide trisodium salt (Thermo Fisher Scientific) were included (100 μg ml^{-1}) in the parenchymal medium and flowed (60 μl h^{-1}) through the upper or basal channel of the chip. The tracers were chosen for low spectral overlap, allowing simultaneous fluorescent quantification, and both tracers were validated for measuring paracellular permeability changes[16]. The concentrations of the tracers were measured in the effluents of the upper (donor, C_D) and lower (receiver, C_R) channels. The apparent permeability formula was derived from a barrier model between donor and receiver microchannels:

$$V_R \frac{dC_R}{dt} = Q_R(C_{R,in} - C_R) - AP_{app}(C_R - C_D) \quad (1)$$

Assuming zero receiver inlet concertation ($C_{Rin} = 0$) and zero initial receiver concentration ($C^0_R = 0$) we can calculate the apparent permeability (P_{app}) as follows:

$$V_R \frac{C_R - 0}{t} = -Q_R C_R - AP_{app}(C_R - C_D) \quad (2)$$

Using the measured concentration at the channel outlets (C_D and C_R) we can calculate the apparent permeability (P_{app}) from the final form:

$$P_{app} = \frac{(V_R/t + Q_R)C_R}{A(C_D - C_R)} \quad (3)$$

where V_R is the volume of the receiving (lower) channel effluent after time t, C_R is the measured concentration of tracer in receiving channel effluent, t is time of effluent collection and A is the area of the barrier. Note that if there is no flow in the receiver channel ($Q_R = 0$), equation (3) simplifies to a classical P_{app} formula for a static barrier.

TEER was measured in Transwells using an EndOhm chamber with an EVOM2 Meter (WPI). The absolute value of TEER can vary depending on the Caco-2 clone used, medium composition and co-culture conditions, as well as the measurement setup. When P_{app} was measured in Transwells, the tracers were added at the same concentrations into the apical compartment as described above, and the Transwells were incubated for 1 h before samples were collected and analysed using a fluorometer. All permeability measurements can vary depending on the device setup as well as the tracer molecular mass; low-molecular-mass tracers are more sensitive to small changes in barrier function. The correlation between TEER and inulin permeability in Caco2 cells has previously been established in multiple publications[47]. TEER electrodes can be integrated into organ chips for real-time measurements[48,49], but these TEER chips are not compatible with the fluidic handling system of the automated culture instrument used here; however, in the future, this approach could be modified for label-free monitoring of barrier function on this system.

Albumin concentrations in samples collected each day from the inlet and outlet channels of the apical and basal channels of the liver chip and kidney chip were quantified using a human albumin ELISA quantitation kit (Bethyl Laboratories). Albumin production and reabsorption were calculated as a rate on the basis of the difference between the inlet and outlet concentrations of apical and basal channels and normalized to total amount of protein.

The activity of cytochrome P450 CYP3A4 within the organ chips was determined using the P450 Glo kit (Promega). In brief, luciferin-IPA was diluted (1:1,000) in the inlet medium of the parenchymal channel and flowed through the organ chip at a rate of 60 μl h^{-1}. After at least 2 h, the chips were purged to collect the remaining metabolite. From these data, the metabolite production rate was determined and standardized to total protein. Total protein was determined in lysates from the parenchymal cells after the endothelium was removed from the basal channel by trypsinization. The remaining cells were dissolved in RIPA buffer supplemented with 1× Halt protease and phosphatase inhibitor single-use cocktail (Thermo Fisher Scientific). Total protein was determined using the Pierce BCA assay kit (Thermo Fisher Scientific). Western blot analysis was performed using 10% Tris-glycine (Novex, WedgeWell, 10-well) gels run at 150 V with protein ladder SeeBlue Plus2 pre-stained protein ladder (Invitrogen). Transfer to nitrocellulose membranes was performed using an iBlot 2 machine (Thermo Fisher Scientific). Primary antibodies against CYP2A6 (Abcam), rabbit P-glycoprotein-1 (141 kDa, Abcam, ab170904; 1:1,000 in 5% BSA in Tris-buffered saline Tween-20 (0.1%) (TBST)), rabbit SLC22A2 (OCT2; 63 kDa, Abcam, ab198800; 1:1,000 in 5% BSA in TBST) and rabbit GAPDH (Cell Signaling, 5174S) 1:10,000 in 5% BSA in TBST were used. Antibodies were visualized using donkey anti-mouse secondary antibodies conjugated to horseradish peroxidase (Jackson ImmunoResearch Laboratories).

To assess bone marrow cell populations, cells from the apical channel were removed by digesting the fibrin gel in buffer containing DMEM supplemented with nattokinase (2.5 mg ml^{-1}, Japan Bio Science Laboratory), 25 mM HEPES (Thermo Fisher Scientific), collagenase type I (1 mg ml^{-1}, Gibco) and 10% FBS for 1 h at 37 °C. The cells were then collected, mixed with 5,000 counting beads (Spherotech) and pelleted by centrifugation at 400*g* for 4 mins at 4 °C. To identify different haematopoietic populations, cells from the apical channel were collected for flow cytometry analysis by digesting the fibrin gel in buffer containing DMEM supplemented with nattokinase (2.5 mg ml^{-1}, Japan Bio Science Laboratory), 25 mM HEPES (Thermo Fisher Scientific), collagenase type I (1 mg ml^{-1}, Gibco) and 10% FBS for 1 h at 37 °C. The cells were then mixed with 5×10^3 counting beads (Spherotech, ACRFP-100–3) to enable quantification of cell numbers. The mixture was pelleted by centrifugation at 400*g* for 4 mins at 4 °C. To identify different haematopoietic populations, surface staining was performed for 30 mins at 4 °C in flow cytometry buffer composed of PBS, 1% FBS, 25 mM HEPES (Thermo Fisher Scientific), 1 mM EDTA (Thermo Fisher Scientific) and 0.05% sodium azide (VWR) using the following antibodies: anti-CD235a-Pacific Blue (HI264 clone, BioLegend, 349108, dilution 1:80), anti-CD15-Brilliant Violet 510 (W6D3 clone, BioLegend, 323028, dilution 1:50) and anti-CD71-PerCP/Cy5.5 (CY1G4 clone, BioLegend, 334114, dilution 1:50) for erythrocytes, and anti-CD16-PE/Dazzle 594 (3G8 clone, BioLegend, 302054, dilution 1:80) and anti-CD13-APC (WM15 clone, BioLegend, 301706, dilution 1:80) for neutrophils, as well as anti-CD34-PE/Cy7 (581 clone, BioLegend, 343516, dilution 1:50) for additional characterization. Furthermore, the staining panel included 20 nM Syto 16 (Thermo Fisher Scientific, S7578), Zombie NIR dye (BioLegend, 423106, dilution: 1:500), Fc Blocker (BioLegend, 422302, dilution 1:20), Monocyte Blocker (BioLegend, 426103, dilution 1:20) and Brilliant Stain Buffer (BD, 566385, dilution 1:20). Data acquisition was performed using a BD LSRFortessa system, and the samples were analysed using FlowJo.

MS was performed by PureHoney Technologies (Billerica). Their RapidFire-MS/MS system consisted of an Agilent RapidFire 300 interfaced to a Sciex API4000 triple quadrupole mass spectrometer using Analyst v.1.6 data acquisition software. All quantitative analysis was performed using Agilent RapidFire Integrator software. Nicotine and cotinine, together with stable isotope internal standards, were simultaneously quantified in positive ion turbospray

mode. Medium samples were diluted such that the maximum concentration was 10 µM or less, which was determined to be upper limit of the linear range of the assay. All of the standard curve injections were performed in triplicate; the limit of detection of the assay ranged from 10 nM to 40 nM. All of the reagents were purchased from Sigma-Aldrich, with the exception of the stable isotope internal standards, which were purchased from Cerilliant. All of the reagents were high performance liquid chromatography (HPLC) grade except for methanol used in Buffer B which was ultra-HPLC grade.

Inductively coupled plasma mass spectrometer (ICP-MS) analysis was performed by PureHoney Technologies (Billerica). The system was composed of an Agilent 7500CX ICP-MS equipped with an ASX-500 autosampler.

Platinum standard solutions (1,000 µg ml^{-1}) were purchased from Agilent Technologies. Trace metal grade nitric acid was purchased from Thermo Fisher Scientific and all water used was HPLC grade.

A mass of 195 was monitored for Pt quantification. A total of three independent measurements of 5.5 s each were performed on each sample and the average instrument response was reported. Then, 40 µl of test sample consisting of cell culture medium was diluted to 4 ml in 2% nitric acid in a 13 × 100 mm polypropylene vial, heated to 50 °C for 30 mins and allowed to cool to room temperature. An eleven-point, 2× serial dilution of Pt starting at 10 µM was prepared as a standard curve and a 12th concentration with 0 p.p.m. Pt was included as a blank. Blank cell culture medium (40 µl) was spiked into each of the 12 standard curve samples to accurately model the test samples

Two separate standard curves, each consisting of six calibration levels, were created for quantitative Pt analysis. A low Pt concentration curve from 0 nM to 10 nM using the pulse detector and a high Pt concentration curve for samples between 10 nM and 1,000 nM using the analogue detector of the 7,500 ICP-MS were generated to analyse the samples. The appropriate standard curve on the basis of the signal level of the test samples (that is, pulse or analogue) was used to calculate the Pt concentration of the test samples. The method had a lower limit of detection below 0.5 nm and was linear to 1,000 nM, the lowest and highest concentration standards tested. Linear curve fitting was used for both the pulse and analogue detector standard curves.

Statistical analysis. A statement of number of replicates is provided in the text for all of the experiments. Data are mean ± s.d. or mean ± s.e.m, as indicated. Significance values were calculated using two-tailed *t*-tests; $P < 0.05$ was considered to be statistically significant.

Bland–Altman analysis was performed for nicotine, cotinine and cisplatin, and is displayed as the average of the MS data and the DMPK model versus the difference between the measured and the modelled data. Furthermore, the IVIVT models were analysed versus the clinical data (geometric mean and s.d.) in a similar manner. The dotted lines show the bias, which is the average of the differences, and the 95% limits of agreement. Correlation analysis was performed using Pearson correlation between measured, MS or clinical data versus the modelled data. Two-tailed tests were performed. Lin's concordance coefficient calculations were also carried out on these datasets. Prism v.8.0 (GraphPad Software) and R environment were used for the Bland–Altman, Pearson correlation and Lin's concordance analysis.

Computational modelling. An overview of the in silico workflow is provided in Supplementary Fig. 15.

Development of models of individual organ chips. DMPK models of each organ chip were developed using ODE-based distributed (spatiotemporal) MCRO fast running models. These models were applied to simulate in vitro ADME and DMPK/PD, in vivo human DMPK/PD and model-based IVIVT. All of the models were developed using CFDRC's Computational Biology (CoBi) tools[50] (http://medicalavatars.cfdrc.com/index.php/cobi-tools/).

Construction of the blank MCRO organ-chip model. The geometry in each MCRO organ-chip model (Fig. 1b,c, Supplementary Figs. 4 and 8) is represented by a coarse spatial computational mesh consists of control volumes in stream-wise direction (PDMS, top channel, epithelial layer, porous membrane, endothelial layer and bottom channel) and one control volume in cross-stream direction (PDMS). The MCRO model is derived for general spatiotemporal transport equations accounting for accumulation, convection, diffusion and reaction:

$$\frac{\partial C}{\partial t} + \nabla(vC) = \nabla(D\nabla C) + S \tag{4}$$

where C is the compound concentration, v is the fluid velocity, D is the diffusion coefficient and S is the generalized source term. The MCRO model is derived from above equation by integrating spatial terms for convection and diffusion into individual fluxes across control volume boundaries and treating them as source terms in the ordinary differential equations. For a simplified barrier configuration (Fig. 1b, Supplementary Fig. 4), the above transport equation, assuming negligible stream-wise diffusion, can be integrated into three ordinary differential equations with the spatial convection and transmembrane diffusive transport terms expressed as individual fluxes:

$$V_B \frac{dC_B}{dt} = Q_B(C_{B,in} - C_B) + J_{B-M} \tag{5}$$

$$V_M \frac{dC_M}{dt} = J_{M-A} - J_{B-M} \tag{6}$$

$$V_A \frac{dC_A}{dt} = Q_A(C_{A,in} - C_A) - J_{M-A} \tag{7}$$

where C_B, C_M and C_A are compound concentrations in individual compartments (basal channel medium, membrane and apical channel medium, respectively), V_B, V_M and V_A are compartment volumes, Q_A and Q_B are the volumetric flow rates in basal and apical microchannels, respectively, and $C_{A,in}$ and $C_{B,in}$ are concentrations at microchannel inlets. The transmembrane fluxes are calculated as follows:

$$J_{B-M} = S\frac{1}{\frac{\delta_M}{k_p D_M} + \frac{\delta_B}{D_B}}\left(\frac{C_M}{k_p} - C_B\right) = S \cdot P_{B-M}\left(\frac{C_M}{k_p} - C_B\right) \tag{8}$$

$$J_{M-A} = S\frac{1}{\frac{\delta_M}{k_p D_M} + \frac{\delta_A}{D_A}}\left(C_A - \frac{C_M}{k_p}\right) = S \cdot P_{M-A}\left(C_A - \frac{C_M}{k_p}\right) \tag{9}$$

where S is the surface area of the barrier (nomenclature not to be confused with the general source term above), P_{B-M} and P_{M-A} are the effective permeability coefficients between compartments and δ represents half of the individual compartment height. Note that depending on the compound partition coefficient k_p there may be a concentration discontinuity at the medium–membrane interfaces (Supplementary Fig. 4, dashed lines). A similar approach was used to calculate fluxes between the channel medium and the PDMS.

Discretization of MCRO organ-chip models and the linked configuration. Each organ chip lined by an epithelium interfaced with an endothelium was further discretized into three axial zones (proximal, central and distal) making the problem two-dimensional, allowing for faster computing compared with whole three-dimensional models. Moreover, this enabled us to calculate both passive and active transport parameters for each organ chip. The MCRO model is therefore segmented into three axial zones, $i = 1,2,3$, in the stream-wise direction (proximal, central and distal) involving convective and diffusive fluxes. For example, for the basal medium (B), three equations are solved:

$$V_{B,i} \frac{dC_{B,i}}{dt} = Q_{B,i}(C_{B,i-1} - C_{B,i}) + \Delta J_{diffB,i} + J_{B-M,i} \tag{10}$$

where $\Delta J_{diff,i}$ is the diffusive flux difference across the downstream and upstream control volume faces in the stream-wise direction (along the microchannel axis):

$$\Delta J_{diffB,i} = \frac{AD}{\Delta x}(C_{B,i+1} - C_{B,i}) - \frac{AD}{\Delta x}(C_{B,i} - C_{B,i-1}) \tag{11}$$

where A is the channel cross-section area and Δx is the channel sub-compartment length. The following sections briefly summarize the transport equation for each organ device.

All of the organ device configurations (that is, gut, liver, kidney and bone marrow chips) have a similar barrier configuration involving several layers: basal PDMS package (BP), basal channel medium (BM), endothelium (E), thin porous PDMS membrane (M), epithelium (H), apical channel medium (AM) and apical PDMS package (AP; Fig. 1c, Supplementary Fig. 4). As a result, all of the organ-chip devices are represented with similar mathematical equations that describe species mass balance in all layers. Specific organ chips were modelled using parameters that are provided in Supplementary Table 8. In the following section, we describe details of the MCRO model that is shared by all of the organ chips used in this study.

MCRO organ-chip model of passive and active transport plus metabolism for calculating intrinsic PK parameters. The organ barrier model for each axial zone ($i = 1,2,3$) in both the individual chip and linked system (Fig. 1b,c) involves compound conservation equations in: basal package, basal medium, endothelial barrier, membrane, epithelial barrier, apical medium and apical package:

$$V_{B,i} \frac{dC_{BP,i}}{dt} = -J_{BP-BM} + \Delta J_{diffBP,i} \tag{12}$$

$$V_{BM,i} \frac{dC_{BM,i}}{dt} = Q_{BP}(C_{BP,i-1} - C_{BM,i}) + J_{BP-BM} - J_{BM-E} + \Delta J_{diff,BM} \tag{13}$$

$$V_{E,i} \frac{dC_{E,i}}{dt} = J_{BM-E} - J_{E-M} \tag{14}$$

$$V_{M,i}\frac{dC_{M,i}}{dt} = J_{E-M} - J_{M-H} + \Delta J_{diff,M,i} \quad (15)$$

$$V_{H,i}\frac{dC_{H,i}}{dt} = J_{M-H} - J_{H-AM} - fu_H \cdot CL_{H,int} \cdot C_{H,i} - k_{act} fu_H C_{H,i} \quad (16)$$

$$V_{AM,i}\frac{dC_{AM,i}}{dt} = Q_{AM}\left(C_{AM,i-1} - C_{AM,i}\right) + J_{H-AM} - J_{AM-AP} + \Delta J_{diff,AM} + k_{act} fu_H C_H \quad (17)$$

$$V_{AP,i}\frac{dC_{AP,i}}{dt} = J_{AM-AP} + \Delta J_{diff,AP,i} \quad (18)$$

where Q_{BM} and Q_{AM} are the medium volumetric flow rates in the basal and apical channels respectively and index, $i = 1,2,3$, represents three stream-wise sections of the organ device (proximal, central and distal). The epithelial cell layer (H) metabolic clearance term in equation (16) with $CL_{H,int}$ represents the intrinsic clearance. The last terms ($k_{cat} fu_H C_{H,i}$) in equations (16) and (17) represent the active transport between the epithelial cells and the apical medium where k_{act} is the efflux rate constant for each different organ chip.

The cross-stream passive diffusion fluxes between individual barrier layers are:

$$J_{BP,BM} = S \cdot P_{BP-BM}\left(fu_{PDMS}\frac{C_{BP,i}}{k_{p,PDMS}} - fu_{Media}C_{BM,i}\right) \quad (19)$$

$$J_{BE,E} = S \cdot P_{BM-E}\left(fu_{Media}C_{BM,i} - fu_E\frac{C_{E,i}}{k_p}\right) \quad (20)$$

$$J_{E-M} = S \cdot P_{E-M}\left(fu_E C_{E,i} - fu_M C_{M,i}\right) \quad (21)$$

$$J_{M-H} = S \cdot P_{M-H}\left(fu_M C_{M,i} - fu_H C_{H,i}\right) \quad (22)$$

$$J_{H-AM} = S \cdot P_{H-AM}\left(fu_H\frac{C_{H,i}}{k_p} - fu_{Media}C_{AM,i}\right) \quad (23)$$

$$J_{AM-AP} = S \cdot P_{AM-AP}\left(fu_{Media}C_{AM,i} - fu_{PDMS}\frac{C_{AP,i}}{k_{p,PDMS}}\right) \quad (24)$$

The stream-wise diffusive flux terms, ΔJ_{diff}, in BM and AM medium, membrane (M) and PDMS package layers (BP, AP) are calculated using equation (11). In the above equations, k_p is the partition coefficient for a specific compound, fu the unbound fraction of the compound in the individual compartments and S is the surface area normal to the cross-stream direction, and P_{BM-BM}, P_{BM-E}, P_{E-M}, P_{M-H}, P_{H-AM} and P_{AM-AP} are the permeabilities for each barrier interface estimated using equations (8) and (9) and then calibrated computationally for each organ device according to the procedure described below.

Calibration of MCRO organ model for compound partition into PDMS. Simulations of the transport of highly lipophilic drugs in organ chips made with the PDMS have to account for drug distribution into the package materials[19]. The MCRO model of each organ chip involves drug conservation equations in the PDMS package layers adjacent to basal and apical channels (equations (12) and (18)). To calculate the medium–PDMS permeability and partition coefficients in flux terms (equations (19) and (24)), we used experimental data that were generated using a blank chip (with no cell layers) perfused with drug in both channels for a specific time period. Experimental drug concentration–time data were collected from the apical and basolateral outlets during the loading. We used the blank organ-chip MCRO model (equations (12), (13), (15), (17) and (18)) with the medium–PDMS partition coefficients and permeabilities as calibration parameters. We used damped least-squares optimization solver in CoBi and Dakota optimization tools (https://dakota.sandia.gov/) to calibrate the parameters. The Dakota toolkit[51], developed by Sandia National Laboratories (available in open source) provides a flexible interface between the analysis solver code (CoBi) and iterative optimization analysis methods. The Dakota framework contains algorithms for optimization with gradient- and non-gradient-based methods; uncertainty quantification with sampling, reliability, stochastic expansion and epistemic methods; parameter estimation with nonlinear least squares methods; and sensitivity/variance analysis with design of experiments and parameter study methods[51]. The described calibrated model has been validated for various hydrophilic and lipophilic test compounds, including FITC-inulin, Dextran Texas Red, and Lucifer Yellow[16]. The calibrated organ-chip MCRO model for a specific compound enables predictive calculation of compound concentrations in the epithelial and endothelial cell compartments, as well as in the barrier, and the associated absorption, metabolism, clearance, toxicity and other PK/PD responses. Moreover, this in silico calibration method enabled us to use a cost effective device fabrication processes and calculate organ-chip PK performance as it would behave in idealized (non-absorbing) designs and materials.

Dynamic organ-chip assumptions in the model. The gut chip is subject to oscillatory membrane/channel stretching[15], which is essential to achieve the in vivo observed physiological functions of the endothelial–epithelial cell barriers in this organ chip[18]. Owing to the low strain and very short time constants of the membrane stretching (~6% strain with 0.15 Hz frequency) compared to the long duration (hours to days) of the PK studies, the direct effects of mechanical strain application on organ geometry can be neglected in the present MCRO organ model. The stretch effects are therefore indirectly accounted for in the calibrated permeability parameters (equations (19)–(24)).

Drug metabolism and modelling metabolite flux. The epithelial layer (H) equation (equation (16)) includes the compound metabolism term calculated using the organ specific intrinsic clearance, $CL_{H,int}$. For example, the equation for the hepatocyte cell layer involves the hepatic intrinsic clearance. For practical cases, conservation equations have to be solved for both the primary compound and for its metabolites. Both sets of equations for both the primary compound and for its metabolites are coupled by the drug metabolism reaction term in the epithelial cell layers (for example, in liver hepatocytes) where a sink term of the primary compound (for example, a prodrug or nicotine) becomes a source term in the equation for the metabolite conservation equation.

MCRO organ-chip model parameters. Each organ chip has its own set of parameters, including channel dimensions, flow rates in the apical and basal channels, and metabolic and transport properties in the organ-specific epithelial cells (intestinal cells in the gut chip, hepatocytes in the liver chip and proximal tubular epithelial cells in the kidney chip). The geometric dimensions that were used to calculate areas (A and S) and volumes for each compartment in equations (12)–(24) for each organ chip are provided in Supplementary Table 1. The cell types used for each organ chip are described in Supplementary Table 2.

The fluidically linked multi-organ-chip model. Computational simulation of fluidically linked organ chips with intermittent medium exchange between the chips involves the above MCRO barrier model equations (equations (12)–(24)) and additional compound conservation equations for four compartments: inlet/outlet tubing and inlet/outlet micro-reservoirs associated with each chip. As the organ micro-reservoirs are periodically emptied and replenished with medium, additional fluid volume conservation equations have to be solved for each micro-reservoir. The conservation equations for the basal and apical side inlet and outlet micro-reservoirs (IR, OR) are as follows (only the basal side is described as both sides have the same equation forms):

$$\frac{dV_{BIR}}{dt} = \dot{V}_{BIR,inj}(t) - Q_{BM} \quad (25)$$

$$\frac{dV_{BIR}C_{BIR}}{dt} = \dot{V}_{BIR,inj}(t)C_{BIR,inj} - Q_{BM}C_{BIR} \quad (26)$$

$$\frac{dV_{BOR}}{dt} = -\dot{V}_{BOR,samp}(t) + Q_{BM} \quad (27)$$

$$\frac{dV_{BOR}C_{BOR}}{dt} = -\dot{V}_{BOR,samp}(t)C_{BOR} + Q_{BM}C_{BOt} \quad (28)$$

where $\dot{V}_{BIR,inj}$ and $\dot{V}_{BOR,samp}$ are the intermittent medium injections into the inlet micro-reservoir from the AV reservoir and sampling from the outlet micro-reservoir, respectively. $C_{BIR,inj}$ is the injected concentration into the inlet basal micro-reservoir (AV reservoir concentration for a linked system) and C_{BOt} is the basal outlet tubing concentration. The inlet/outlet tubing (It, Ot) equations are:

$$V_{BIt}\frac{dC_{BIt}}{dt} = Q_{BM}\left(C_{BIR} - C_{BIt}\right) \quad (29)$$

$$V_{BOt}\frac{dC_{BOt}}{dt} = Q_{BM}\left(C_{BI,3} - C_{BOt}\right) \quad (30)$$

where $C_{BI,3}$ is the concentration at the basal medium outlet section ($i = 3$, in equation (13)). The conservation equations for the apical side have similar form. As the time scale of the intermittent medium exchange in micro-reservoirs (a few minutes) is much smaller than the organ operation time sale (several hours), the above equations can be expressed as algebraic equations for mass balance in micro-reservoirs before and after the sampling event. Two linked organ systems have been simulated using the above MCRO organ-chip models:

- Gut, liver and kidney chips to study gut (oral) nicotine absorption, hepatic metabolism, and systemic liver and renal clearance (Figs. 1 and 2).

- Liver, kidney and bone marrow chips to investigate intravenous cisplatin administration, systemic PK and PD effects on bone marrow haematopoietic stem cells (Fig. 4).

The major difference is the route of drug administration—oral through the gut for the nicotine studies and intravenous into the AV reservoir for cisplatin.

For the nicotine system simulations, the flow path of the basal medium between individual organ chips and the AV reservoir, which collects medium from basal micro-reservoir outlets from all organ chips, is shown in Fig. 1a,c. The liver chip inlet micro-reservoir was supplied from the gut chip basal outlet micro reservoir (representing a portal vein) and from the AV reservoir (representing the hepatic artery). The medium transferred to the kidney chip was divided into two paths—the glomerular filtrate flow and the glomerular efferent arteriole flow supplying the kidney tubular channel. A virtual glomerulus model was applied in both the experimental and computational systems by extracting a medium volume filtered by the virtual glomerulus into the filtrate path (apical epithelial channel of the kidney chip), and the rest was supplied to the medium inlet mini-reservoir of the basal vascular channel. The filtrate flow rate was calculated on the basis of renal physiological data and compound physicochemical properties. A similar medium circulation pattern was used for modelling the cisplatin system, except the gut chip was replaced by the bone marrow chip. In this case, owing to a lack of a gut chip, the inlet mini-reservoir of the basal vascular channel of the liver chip was fully supplied with blood-substitute medium directly from the AV reservoir.

Simulating the AV compartment. The physiological AV pool is represented by the AV reservoir with a dynamic medium volume, $V_{AV}(t)$, which was periodically resupplied from the basal (venous) outlet micro-reservoirs of the liver and kidney chips, drained to supply inlet micro-reservoirs of the basal vascular channels of all organ-chip devices, replenished with fresh medium and sampled for analysis. The total and compound mass balance equations describe the AV reservoir dynamics:

$$\frac{dV_{AV}}{dt} = -\left(\dot{V}_{BIR,g} + \dot{V}_{BIR,l} + \dot{V}_{BIR,k} + \dot{V}_{AIR,k} + \dot{V}_{sM}\right) + \dot{V}_{BOR,l} + \dot{V}_{BOR,k} + \dot{V}_{fM} \quad (31)$$

$$\frac{d(V_{AV}C_{AV})}{dt} = -\left(\dot{V}_{BIR,g} + \dot{V}_{BIR,l} + \dot{V}_{BIR,k} + \dot{V}_{AIR,k} + \dot{V}_{sM}\right)C_{AV} + \dot{V}_{BOR,l}C_{BOR,l} + \dot{V}_{BOR,k}C_{BOR,k} + \dot{V}_{fM}C_{fM} \quad (32)$$

where the indices g, l, k and fM stand for gut, liver, kidney and fresh medium, respectively. $\dot{V}_{sM}$ and $\dot{V}_{fM}$ are the volumetric rates of sampling and fresh medium supply to the AV reservoir. As for the micro-reservoirs, the above equations can be expressed as algebraic mass balance equations in the AV reservoir before and after the sampling event. In the nicotine studies, pure medium was injected, $C_{fM}=0$, (experimentally delivered to the gut); by contrast, for the cisplatin study, the drug was supplied at a specified concentration, $C_{fM}>0$ to mimic IV infusion experimentally.

Solving MCRO simulations. The above system of ODE equations for each organ was programmed in the form of text (.SIM) input files and solved using CoBi tools, using a standard PC workstation. These tools and instructions for running simulation solvers are available at http://medicalavatars.cfdrc.com/index.php/cobi-tools//.

Implementation of IVIVT of human PK parameters. Even the most advanced in vitro human-body-on-chip (HuBoC) systems are an enormous simplification of the human body. Thus, there will always be a need for mathematical model-based extrapolation of in vitro results to humans in vivo. In vitro-to-in vivo correlation described previously involves a predictive mathematical model that describes the relationship between an in vitro property of a dosage form and an in vivo response[2]. This dose-response model establishes a statistical correlation between in vitro dissolution or permeation rate and in vivo PK properties such as C_{max} and AUC[52,53], but it does not quantitatively predict these parameters. By contrast, IVIVE applies mechanistic, but relatively simple, models to extrapolate the in vitro drug metabolism in cell cultures or transport across barriers to in vivo organ clearance or absorption[54,55]. In vitro organ data along with drug physicochemical properties are then used in PBPK models[56,57]. Physiologically interconnected multi-organ-chip systems such as the one described here can generate huge amounts of data that require new computational tools for both interpretation of in vitro data and for translation to humans in vivo (IVIVT)[9,58]. Here we used multiphysics CoBi tools for first-principles-based modelling of multiple fluidically linked organ chips and to develop a quantitative IVIVT approach.

Conventional IVIVE methods rely on static cell culture or barrier experiments to estimate single lumped PK parameters in vivo using in vitro data. Separate in vitro experiments are used to estimate drug dissolution, intestinal permeability (absorption)[59], hepatic intrinsic clearance[25,60] or renal clearance rates[25]. For example, the in vivo hepatic clearance CL_h and the hepatic availability ($F_h=1-CL_h/Q_h$) can be calculated using in vitro primary human hepatocytes culture data and the well-stirred liver model as described previously[61,62]:

$$CL_h = \frac{Q_h \cdot fu_p \cdot CL_{int,in\ vivo}}{Q_h + fu_p \cdot CL_{int,in\ vivo}} \quad (33)$$

where Q_h is the liver blood flow (20 ml min^{-1} kg^{-1}), fu_p is the unbound fraction in plasma and the in vivo clearance is estimated using a physiology-based scaling factor SF that converts the units of $CL_{int,in\ vitro}$ (μl min^{-1} per 10^6 cells) to $CL_{int,in\ vivo}$ (ml min^{-1} kg^{-1}):

$$CL_{int,in\ vivo} = CL_{int,in\ vitro} \times SF = CL_{int,in\ vitro} \times HPGL \times LiverWt \times REF \quad (34)$$

where HPGL is the hepatocellularity (that is, the number of hepatocytes per gram of liver = 99–120 × 10^6). LiverWt is the liver weight (1,500–1,800 g liver per 70 kg) and REF is the relative expression factor (a ratio of in vivo/in vitro expression of metabolic enzymes or transporters; often, REF ≈ 1)[61,63]. The scaled intrinsic clearance can then be used as a sink term for the liver compartment in the in vivo PBPK model[33,61,62].

Complementary experimental and computational models of in vitro physiologically connected organ chips provide a unique opportunity to establish next-generation multiscale PBPK models that couple the whole body with spatially and morphologically resolved barrier models[64–66]. It has been proposed that computational models of morphologically resolved barriers in organs (gut, liver, lung, brain, kidney, skin and bone) that are validated in vitro in organ chip and multiple-linked HuBoC systems could be directly applied in barrier-resolved multiscale PBPK models. Here, we integrated computational models of organ chips with functionalized barriers, calibrated and validated on experimental data, to construct corresponding spatially resolved in vivo barrier models within a multiscale PBPK framework, such as that incorporated in CoBi tools[66], to develop a quantitative IVIVT protocol.

Comparison with other organ-chip models. The key design principle for organ chips is to recapitulate in vitro anatomical, physiological and PK parameters exhibited by living tissue barriers within living organs in vivo. Previous models of fluidically perfused organ-chip designs represent the tissue barrier in the form of vertically stacked barriers[18], horizontally stacked barriers or Transwells with fluidic connection to perfusion chambers[56]. As discussed above, each approach has some advantages and limitations; however, from the computational model point of view, the parallel channels and Transwell designs have considerable disadvantages. Note that, in past formulations, the liver model is subdivided into two compartments—basal and apical—and the hepatocytes are lumped in with the apical compartment[56]. In the open surface Transwell device, the apical volume is treated as time dependent. In other previously described models[40,67], the liver model was represented as a single well-stirred reactor with medium flowing across the barrier and the clearance term applied to the entire liver volume rather than the hepatocyte cell layer. The model described here contained an additional hepatocyte compartment.

One of the goals of this study was to explore how to adapt the in silico model of the in vitro linked multi-organ chip to achieve compound DMPK profiles observed in humans in vivo. To evaluate the feasibility of a potential IVIVT protocol, we decided to retain the in vitro MCRO model of the barrier between the basal and apical medium, but we explored adaptation and scaling of other components of the in silico model as well, including:

- Connecting all organs microfluidically with continuous, rather than intermittent, medium exchange to emulate physiological conditions.
- Directly connecting individual organ chips to an AV reservoir (that is, basal venous outlets supplying the AV reservoir), which then feeds basal arterial inlets.
- Adjusting the geometry of microfluidic channels to replicate more physiological conditions by increasing the surface area, decreasing channel height and scaling the organ vascular volume to achieve human values (as in typical PBPK models; Fig. 3c).
- Calibrating the flow-rate ratios through the organ chips to achieve physiological flow distribution exhibited by those organs in vivo (as in human PBPK models on the basis of Supplementary Table 4).
- Calibrating the AV reservoir volume to account for missing organs and tissues (such as fat) and for drug-specific volume of distribution.

With these modifications of the modelling approach, we were able to computationally reproduce the in vivo PK profiles of human clinical data for both nicotine and cisplatin at different doses and different routes of administration.

Reporting Summary. Further information on research design is available in the Nature Research Reporting Summary linked to this article.

Data availability

All data supporting the results in this study are available within the Article and its Supplementary Information. The broad range of raw datasets acquired and analysed (or any subsets of it), which for reuse would require contextual metadata, are available from the corresponding author on reasonable request.

Code availability

The CoBi code used to simulate individual organs and their network, as well as individual organ models, is freely available at http://medicalavatars.cfdrc.com/

index.php/cobi-tools, under the folder 'Microphysiological Organs and Systems Models'.

Received: 22 May 2019; Accepted: 25 November 2019;
Published online: 27 January 2020

References

1. Shanks, N., Greek, R. & Greek, J. Are animal models predictive for humans? *Philos. Ethics Humanit. Med.* **4**, 2 (2009).
2. Malinowski, H. et al. Draft guidance for industry extended-release solid oral dosage forms. Development, evaluation and application of in vitro-in vivo correlations. *Adv. Exp. Med. Biol.* **423**, 269–288 (1997).
3. Danhof, M., de Lange, E. C. M., Della Pasqua, O. E., Ploeger, B. A. & Voskuyl, R. A. Mechanism-based pharmacokinetic-pharmacodynamic (PK-PD) modeling in translational drug research. *Trends Pharmacol. Sci.* **29**, 186–191 (2008).
4. Abaci, H. E. & Shuler, M. L. Human-on-a-chip design strategies and principles for physiologically based pharmacokinetics/pharmacodynamics modeling. *Integr. Biol.* **7**, 383–391 (2015).
5. Esch, M. B., Ueno, H., Applegate, D. R. & Shuler, M. L. Modular, pumpless body-on-a-chip platform for the co-culture of GI tract epithelium and 3D primary liver tissue. *Lab Chip* **16**, 2719–2729 (2016).
6. Coppeta, J. R. et al. A portable and reconfigurable multi-organ platform for drug development with onboard microfluidic flow control. *Lab Chip* **17**, 134–144 (2016).
7. Xiao, S. et al. A microfluidic culture model of the human reproductive tract and 28-day menstrual cycle. *Nat. Commun.* **8**, 14584 (2017).
8. Wagner, I. et al. A dynamic multi-organ-chip for long-term cultivation and substance testing proven by 3D human liver and skin tissue co-culture. *Lab Chip* **13**, 3538–3547 (2013).
9. Stokes, C. L., Cirit, M. & Lauffenburger, D. A. Physiome-on-a-Chip: the challenge of "scaling" in design, operation, and translation of microphysiological systems. *CPT Pharmacomet. Pharmacol.* **4**, 559–562 (2015).
10. Bovard, D. et al. A lung/liver-on-a-chip platform for acute and chronic toxicity studies. *Lab Chip* **18**, 3814–3829 (2018).
11. Oleaga, C. et al. Multi-organ toxicity demonstration in a functional human in vitro system composed of four organs. *Sci. Rep.* **6**, 20030 (2016).
12. Maschmeyer, I. et al. A four-organ-chip for interconnected long-term co-culture of human intestine, liver, skin and kidney equivalents. *Lab Chip* **15**, 2688–2699 (2015).
13. Edington, C. D. et al. Interconnected microphysiological systems for quantitative biology and pharmacology Studies. *Sci. Rep.* **8**, 4530 (2018).
14. Vernetti, L. et al. Functional coupling of human microphysiology systems: intestine, liver, kidney proximal tubule, blood-brain barrier and skeletal muscle. *Sci. Rep.* **7**, 42296 (2017).
15. Kim, H. J., Li, H., Collins, J. J. & Ingber, D. E. Contributions of microbiome and mechanical deformation to intestinal bacterial overgrowth and inflammation in a human gut-on-a-chip. *Proc. Natl Acad. Sci. USA* **113**, E7–E15 (2016).
16. Novak, R. et al. Robotic fluidic coupling and interrogation of multiple vascularized organ chips. *Nat. Biomed. Eng.* https://doi.org/10.1038/s41551-019-0497-x (2020).
17. Jang, K.-J. et al. Human kidney proximal tubule-on-a-chip for drug transport and nephrotoxicity assessment. *Integr. Biol.* **5**, 1119–1129 (2013).
18. Prantil-Baun, R. et al. Physiologically based pharmacokinetic and pharmacodynamic analysis enabled by microfluidically linked organs-on-chips. *Annu. Rev. Pharmacol. Toxicol.* **58**, 37–64 (2018).
19. Auner, A. W., Tasneem, K. M., Markov, D. A., McCawley, L. J. & Hutson, M. S. Chemical-PDMS binding kinetics and implications for bioavailability in microfluidic devices. *Lab Chip* **19**, 864–874 (2019).
20. Jalili-Firoozinezhad, S. et al. A complex human gut microbiome cultured in an anaerobic intestine-on-a-chip. *Nat. Biomed. Eng.* **3**, 520–531 (2019).
21. Kasendra, M. et al. Development of a primary human small intestine-on-a-chip using biopsy-derived organoids. *Sci. Rep.* **8**, 2871 (2018).
22. Kim, H. J., Huh, D., Hamilton, G. & Ingber, D. E. Human gut-on-a-chip inhabited by microbial flora that experiences intestinal peristalsis-like motions and flow. *Lab Chip* **12**, 2165–2174 (2012).
23. Jang, K.-J. et al. Reproducing human and cross-species toxicities using a Liver-Chip. *Science Transl. Med.* **11**, eaax5516 (2019).
24. Pullan, R. D. et al. Transdermal nicotine for active ulcerative colitis. *N. Engl. J. Med.* **330**, 811–815 (1994).
25. Benowitz, N. L., Hukkanen, J. & Jacob, P. Nicotine chemistry, metabolism, kinetics and biomarkers. *Handb. Exp. Pharmacol.* **192**, 29–60 (2009).
26. Dancik, Y., Anissimov, Y. G., Jepps, O. G. & Roberts, M. S. Convective transport of highly plasma protein bound drugs facilitates direct penetration into deep tissues after topical application. *Br. J. Clin. Pharm.* **73**, 564–578 (2012).
27. Varma, M. V. S. et al. Physicochemical determinants of human renal clearance. *J. Med. Chem.* **52**, 4844–4852 (2009).
28. Digard, H., Proctor, C., Kulasekaran, A., Malmqvist, U. & Richter, A. Determination of nicotine absorption from multiple tobacco products and nicotine gum. *Nicotine Tob. Res.* **15**, 255–261 (2013).
29. Prytz, H., Benoni, C. & Tagesson, C. Does smoking tighten the gut? *Scand. J. Gastroenterol.* **24**, 1084–1088 (1989).
30. Suenaert, P. et al. In vivo influence of nicotine on human basal and NSAID-induced gut barrier function. *Scand. J. Gastroenterol.* **38**, 399–408 (2003).
31. McGilligan, V. E., Wallace, J. M. W., Heavey, P. M., Ridley, D. L. & Rowland, I. R. The effect of nicotine in vitro on the integrity of tight junctions in Caco-2 cell monolayers. *Food Chem. Toxicol.* **45**, 1593–1598 (2007).
32. Rodriguez-Gaztelumendi, A., Alvehus, M., Andersson, T. & Jacobsson, S. O. P. Comparison of the effects of nicotine upon the transcellular electrical resistance and sucrose permeability of human ECV304/rat C6 co-cultures and human CaCo2 cells. *Toxicol. Lett.* **207**, 1–6 (2011).
33. Jones, H. M. & Rowland-Yeo, K. Basic concepts in physiologically based pharmacokinetic modeling in drug discovery and development. *CPT Pharmacomet. Pharmacol.* **2**, 1–12 (2013).
34. Yamazaki, H. et al. Human blood concentrations of cotinine, a biomonitoring marker for tobacco smoke, extrapolated from nicotine metabolism in rats and humans and physiologically based pharmacokinetic modeling. *Int. J. Environ. Res. Publ. Health* **7**, 3406–3421 (2010).
35. Hartmann, J. T. & Lipp, H.-P. Toxicity of platinum compounds. *Expert Opin. Pharmacother.* **4**, 889–901 (2003).
36. Chou, D. B. et al. On-chip recapitulation of clinical bone marrow toxicities and patient-specific pathophysiology. *Nat. Biomed. Eng.* https://doi.org/10.1038/s41551-019-0495-z (2020).
37. Sparreboom, A., Nooter, K., Loos, W. J. & Verweij, J. The (ir)relevance of plasma protein binding of anticancer drugs. *Neth. J. Med.* **59**, 196–207 (2001).
38. Rajkumar, P. et al. Cisplatin concentrations in long and short duration infusion: implications for the optimal time of radiation delivery. *J. Clin. Diagn. Res.* **10**, XC01–XC04 (2016).
39. Wikswo, J. P. et al. Scaling and systems biology for integrating multiple organs-on-a-chip. *Lab Chip* **13**, 3496–3511 (2013).
40. Maass, C., Stokes, C. L., Griffith, L. G. & Cirit, M. Multi-functional scaling methodology for translational pharmacokinetic and pharmacodynamic applications using integrated microphysiological systems (MPS). *Integr. Biol.* **9**, 290–302 (2017).
41. Neault, J. F. & Tajmir-Riahi, H. A. Interaction of cisplatin with human serum albumin. Drug binding mode and protein secondary structure. *Biochim. Biophys. Acta* **1384**, 153–159 (1998).
42. Vickers, A. E. M. et al. Kidney slices of human and rat to characterize cisplatin-induced injury on cellular pathways and morphology. *Toxicol. Pathol.* **32**, 577–590 (2004).
43. Huang, Q. et al. Assessment of cisplatin-induced nephrotoxicity by microarray technology. *Toxicol. Sci.* **63**, 196–207 (2001).
44. Maass, C. et al. Establishing quasi-steady state operations of microphysiological systems (MPS) using tissue-specific metabolic dependencies. *Sci. Rep.* **8**, 8015 (2018).
45. Huh, D. et al. Microfabrication of human organs-on-chips. *Nat. Protoc.* **8**, 2135–2157 (2013).
46. Park, T. -E. et al. Hypoxia-enhanced blood-brain barrier chip recapitulates human barrier function, drug penetration, and antibody shuttling properties. *Nat. Commun.* **10**, 2621 (2019).
47. Elamin, E. E. et. al. in *Molecular Aspects of Alcohol and Nutrition: A Volume in the Molecular Nutrition Series* (ed. Patel, V. B.) Ch. 14 (Elsevier, 2016).
48. Henry, O. Y. F. et al. Organs-on-chips with integrated electrodes for trans-epithelial electrical resistance (TEER) measurements of human epithelial barrier function. *Lab Chip* **17**, 2264–2271 (2017).
49. Maoz, B. M. et al. Organs-on-Chips with combined multi-electrode array and transepithelial electrical resistance measurement capabilities. *Lab Chip* **17**, 2294–2302 (2017).
50. Przekwas, A., Friend, T., Teixeira, R., Chen, Z. & Wilkerson, P. *Spatial Modeling Tools for Cell Biology* (Air Force Research Laboratory Information Directorate Rome Research Site, 2006).
51. Adams, B. M. et al. *Dakota, a Multilevel Parallel Object-Oriented Framework for Design Optimization, Parameter Estimation, Uncertainty Quantification, and Sensitivity Analysis* (OSTI, 2014).
52. Amidon, G. L., Lennernäs, H., Shah, V. P. & Crison, J. R. A theoretical basis for a biopharmaceutic drug classification: the correlation of in vitro drug product dissolution and in vivo bioavailability. *Pharm. Res.* **12**, 413–420 (1995).
53. O'Hara, T. et al. In vivo-in vitro correlation (IVIVC) modeling incorporating a convolution step. *J. Pharmacokinet. Pharmacodyn.* **28**, 277–298 (2001).
54. Howell, B. A. et al. In vitro to in vivo extrapolation and species response comparisons for drug-induced liver injury (DILI) using DILIsym™: a mechanistic, mathematical model of DILI. *J. Pharmacokinet. Pharmacodyn.* **39**, 527–541 (2012).
55. Poulin, P. & Haddad, S. Toward a new paradigm for the efficient in vitro-in vivo extrapolation of metabolic clearance in humans from hepatocyte data. *J. Pharm. Sci.* **102**, 3239–3251 (2013).

56. Chen, Y., Jin, J. Y., Mukadam, S., Malhi, V. & Kenny, J. R. Application of IVIVE and PBPK modeling in prospective prediction of clinical pharmacokinetics: strategy and approach during the drug discovery phase with four case studies. *Biopharm. Drug Dispos.* **33**, 85–98 (2012).
57. Rostami-Hodjegan, A. Physiologically based pharmacokinetics joined with in vitro-in vivo extrapolation of ADME: a marriage under the arch of systems pharmacology. *Clin. Pharmacol. Ther.* **92**, 50–61 (2012).
58. Cirit, M. & Stokes, C. L. Maximizing the impact of microphysiological systems with in vitro-in vivo translation. *Lab Chip* **18**, 1831–1837 (2018).
59. Zhu, C., Jiang, L., Chen, T.-M. & Hwang, K.-K. A comparative study of artificial membrane permeability assay for high throughput profiling of drug absorption potential. *Eur. J. Med. Chem.* **37**, 399–407 (2002).
60. Hukkanen, J., Jacob, P. & Benowitz, N. L. Metabolism and disposition kinetics of nicotine. *Pharmacol. Rev.* **57**, 79–115 (2005).
61. Riley, R. J., McGinnity, D. F. & Austin, R. P. A unified model for predicting human hepatic, metabolic clearance from in vitro intrinsic clearance data in hepatocytes and microsomes. *Drug Metab. Dispos.* **33**, 1304–1311 (2005).
62. Chiba, M., Ishii, Y. & Sugiyama, Y. Prediction of hepatic clearance in human from in vitro data for successful drug development. *AAPS J.* **11**, 262–276 (2009).
63. Jamei, M. et al. A mechanistic framework for in vitro-in vivo extrapolation of liver membrane transporters: prediction of drug-drug interaction between rosuvastatin and cyclosporine. *Clin. Pharmacokinet.* **53**, 73–87 (2014).
64. Sluka, J. P. et al. A liver-centric multiscale modeling framework for xenobiotics. *PLoS ONE* **11**, e0162428 (2016).
65. Clancy, C. E. et al. Multiscale modeling in the clinic: drug design and development. *Ann. Biomed. Eng.* **44**, 2591–2610 (2016).
66. Kannan, R. R., Singh, N. & Przekwas, A. A compartment-quasi-3D multiscale approach for drug absorption, transport, and retention in the human lungs. *Int. J. Numer. Method Biomed. Eng.* **34**, e2955 (2018).
67. Tsamandouras, N. et al. Integrated gut and liver microphysiological systems for quantitative in vitro pharmacokinetic studies. *AAPS J.* **19**, 1499–1512 (2017).
68. Gong, C. et al. Hepatotoxicity and pharmacokinetics of cisplatin in combination therapy with a traditional Chinese medicine compound of Zengmian Yiliu granules in ICR mice and SKOV-3-bearing nude mice. *BMC Complement. Altern. Med.* **15**, 283 (2015).

Acknowledgements

We thank M. Rosnach for his artwork, B. Fountaine and S. Kroll for their help with photography, N. Dimitrakakis for statistical analysis and C. Vidoudez for MS analysis. This research was sponsored by the Wyss Institute for Biologically Inspired Engineering at Harvard University, the Defense Advanced Research Projects Agency under cooperative agreement no. W911NF-12-2-0036 and US Food and Drug Administration grant HHSF223201310079C. Funding from Knut och Alice Wallenberg's stiftelse (grant no. 2015-0178; to A.H.) is acknowledged. The views and conclusions contained in this document are those of the authors and should not be interpreted as representing the official policies, either expressed or implied, of the Defense Advanced Research Projects Agency, or the US Government. This work was performed in part at the Center for Nanoscale Systems (CNS), a member of the National Nanotechnology Coordinated Infrastructure Network, which is supported by the National Science Foundation under award no. 1541959. The CNS is part of Harvard University, the Harvard Materials Research Science and Engineering Center (DMR-1420570).

Author contributions

A.H., B.M.M., R.N. and R.P.-B. helped to design and manage the multi-organ linking studies, led the data analysis for generation of figures as well as assembly of the manuscript with D.E.I. D.D., M.R.S. and A.P. were responsible for DM-PBPK/PD model development and data analysis working closely with A.H., B.M.M., R.P.-B. and R.N. A.H., B.M.M., M.C., T.H. and S.S.F.J. planned and performed biological experiments with the help of R.N., Y.M., B.S., A.S.P. and S.J.-F., all under the supervision of O.L., A.C., R.N., R.P.-B., K.K.P. and D.E.I. R.N., B.C., K.K.P. and D.E.I. were responsible for chip development and fabrication. M.I., S.M, A.D. and R.N. were responsible for software and hardware engineering and operation of the linking studies. R.P.-B., R.N., K.K.P. and D.E.I. were responsible for overseeing the entire effort, including preparation of the manuscript.

Competing interests

D.E.I. is a founder and holds equity in Emulate, and chairs its scientific advisory board. K.K.P. is a consultant to Emulate. S.S.F.J. is an employee of and holds equity in Emulate. M.C., A.H., D.E.I., M.I., O.L., B.M.M., Y.M., R.N., K.K.P., A.S.-P. and D.E.I. are listed as inventors on intellectual property licensed to Emulate. The remaining authors declare no competing interests.

Additional information

Supplementary information is available for this paper at https://doi.org/10.1038/s41551-019-0498-9.

Correspondence and requests for materials should be addressed to D.E.I.

nature research

Corresponding author(s): Donald Ingber

Last updated by author(s): Feb 20, 2019

Reporting Summary

Nature Research wishes to improve the reproducibility of the work that we publish. This form provides structure for consistency and transparency in reporting. For further information on Nature Research policies, see Authors & Referees and the Editorial Policy Checklist.

Statistics

For all statistical analyses, confirm that the following items are present in the figure legend, table legend, main text, or Methods section.

n/a	Confirmed	
☐	☒	The exact sample size (*n*) for each experimental group/condition, given as a discrete number and unit of measurement
☐	☒	A statement on whether measurements were taken from distinct samples or whether the same sample was measured repeatedly
☐	☒	The statistical test(s) used AND whether they are one- or two-sided *Only common tests should be described solely by name; describe more complex techniques in the Methods section.*
☒	☐	A description of all covariates tested
☐	☒	A description of any assumptions or corrections, such as tests of normality and adjustment for multiple comparisons
☐	☒	A full description of the statistical parameters including central tendency (e.g. means) or other basic estimates (e.g. regression coefficient) AND variation (e.g. standard deviation) or associated estimates of uncertainty (e.g. confidence intervals)
☐	☒	For null hypothesis testing, the test statistic (e.g. *F*, *t*, *r*) with confidence intervals, effect sizes, degrees of freedom and *P* value noted *Give P values as exact values whenever suitable.*
☒	☐	For Bayesian analysis, information on the choice of priors and Markov chain Monte Carlo settings
☒	☐	For hierarchical and complex designs, identification of the appropriate level for tests and full reporting of outcomes
☒	☐	Estimates of effect sizes (e.g. Cohen's *d*, Pearson's *r*), indicating how they were calculated

Our web collection on statistics for biologists contains articles on many of the points above.

Software and code

Policy information about availability of computer code

Data collection	No software was used.
Data analysis	Excel and Graphpad Prism were used. CFDRC's CoBI tools were used for pharmacokinetic modelling. The CoBi code used to simulate individual organs and their network, as well as individual organ models, are freely available at http://medicalavatars.cfdrc.com/index.php/cobi-tools, under the folder 'Microphysiological Organs and Systems Models'.

For manuscripts utilizing custom algorithms or software that are central to the research but not yet described in published literature, software must be made available to editors/reviewers. We strongly encourage code deposition in a community repository (e.g. GitHub). See the Nature Research guidelines for submitting code & software for further information.

Data

Policy information about availability of data

All manuscripts must include a data availability statement. This statement should provide the following information, where applicable:

- Accession codes, unique identifiers, or web links for publicly available datasets
- A list of figures that have associated raw data
- A description of any restrictions on data availability

All the data supporting the results in this study are available within the Article and its Supplementary Information. The broad range of raw datasets acquired and analysed (or any subsets of it), which for reuse would require contextual metadata, are available from the corresponding author on reasonable request.

Field-specific reporting

Please select the one below that is the best fit for your research. If you are not sure, read the appropriate sections before making your selection.

☒ Life sciences ☐ Behavioural & social sciences ☐ Ecological, evolutionary & environmental sciences

For a reference copy of the document with all sections, see nature.com/documents/nr-reporting-summary-flat.pdf

Life sciences study design

All studies must disclose on these points even when the disclosure is negative.

Sample size	The sample size for the linkage experiment was determined on the basis of the capacity limitations of the instrumentation. The interrogator instrument holds 10 different organ chips, and we built 2 interrogator instruments that were used in these studies. Thus, we were limited to 3 chips of each organ type for each 3-organ-linking study + 1 AV reservoir.
Data exclusions	Data were not excluded from the experiments included in the paper.
Replication	Replication of the experimental findings failed on a few occasions, owing to: 1) Hardware–software communication errors. 2) Human errors of setting up the experiments. 3) Bacterial infections. Organ-chip systems are inherently more susceptible to infections owing to the large number of interfaces. Experiments that suffered from any of the above mentioned problems were not included in the manuscript.
Randomization	Organ chips were randomly distributed into control and treated groups.
Blinding	Samples were not blinded.

Reporting for specific materials, systems and methods

We require information from authors about some types of materials, experimental systems and methods used in many studies. Here, indicate whether each material, system or method listed is relevant to your study. If you are not sure if a list item applies to your research, read the appropriate section before selecting a response.

Materials & experimental systems

n/a	Involved in the study
☐	☒ Antibodies
☐	☒ Eukaryotic cell lines
☒	☐ Palaeontology
☒	☐ Animals and other organisms
☒	☐ Human research participants
☒	☐ Clinical data

Methods

n/a	Involved in the study
☒	☐ ChIP-seq
☒	☐ Flow cytometry
☒	☐ MRI-based neuroimaging

Antibodies

Antibodies used	The following primary antibodies were used for immunocytochemistry experiments: mouse anti-vascular endothelial (VE)-cadherin (Abcam, Cambridge, MA, USA 1:100), mouse anti-vascular endothelial (VE)-cadherin (Abcam, Cambridge, UK, 1:100), Purified mouse anti-human CD-144 Clone 55-7H1(RUO), (VE)-cadherin (BD Biosciences, USA 1:100, Cat # BD555661, Lot #4324666), alpha-actinin (Abcam, Cambridge, UK, 1:200), 0), mouse anti-zona occludens-1 (ZO-1) (Invitrogen 1:100, cat# 33-9100), .] anti-CD235a-Pacific Blue (HI264 clone, BioLegend, 349108, dilution 1:80), anti-CD15-Brilliant Violet 510 (W6D3 clone, BioLegend, 323028, dilution 1:50) and anti-CD71-PerCP/Cy5.5 (CY1G4 clone, BioLegend, 334114, dilution 1:50) for erythrocytes and anti-CD16-PE/Dazzle 594 (3G8 clone, BioLegend, 302054, dilution 1:80) and anti-CD13-APC (WM15 clone, BioLegend, 301706, dilution 1:80) for neutrophils, as well as anti-CD34-PE/Cy7 (581 clone, BioLegend, 343516, dilution 1:50) for additional characterization.The secondary antibodies were anti-rabbit or anti-mouse IgG conjugated with Alexa Fluor-488, Alexa Fluor-555, or Alexa Fluor-647 (Invitrogen, Carlsbad, CA, USA). Hoechst (10 mg/ml, 33342, Life Technologies\ Invitrogen, Carlsbad, CA, USA) was used at a dilution of 1:5000 for nuclei staining. For staining of F-actin, Alexa Fluor-488-phalloidin (Cat# A12379 Lot# 1583098) or Alexa Fluor-647-phalloidin (Life Sciences/Invitrogen, Carlsbad, CA, USA) were used at dilution of 1:30.
Validation	All validation statements are taken from supplier websites. 1. Based on immunoelectrophoresis and/or ELISA, the antibody reacts with the Fc portion of mouse IgG heavy chain but not with the Fab portion of mouse immunoglobulins. No antibody was detected against mouse IgM or against non-immunoglobulin serum proteins. The antibody may cross-react with immunoglobulins from other species. 2. Based on immunoelectrophoresis and/or ELISA, the antibody reacts with whole molecule mouse IgG. It also reacts with the light chains of other mouse immunoglobulins. No antibody was detected against non-immunoglobulin serum proteins. The

antibody has been tested by ELISA and/or solid-phase adsorbed to ensure minimal cross-reaction with bovine, chicken, goat, guinea pig, syrian hamster, horse, human, rabbit, rat and sheep serum proteins, but it may cross-react with immunoglobulins from other species.
3. The antibody has been solid-phase absorbed with human and cow serum proteins.
In crossed immunoelectrophoresis using 50 µL antibody per cm2 gel area, no reaction with 2 µL human plasma and 2 µL cow serum is observed. Staining: Coomassie Brilliant Blue.
In indirect ELISA, the antibody shows no reaction with human plasma and cow serum.
4. Immunogen synthetic peptide corresponding to Human VE Cadherin aa 750 to the C-terminus conjugated to keyhole limpet haemocyanin.(Peptide available as ab27462). This antibody gave a positive signal in HUVEC (Human umbilical vein epithelial) Cell Lysate in Western blot, and in confluent HUVEC cells in ICC/IF.
5. Immunogen: Full length SDS denatured protein (purified from pheochromocytoma) (Rat).

Eukaryotic cell lines

Policy information about cell lines

Cell line source(s)	Caco-2 BBe cells were acquired from Harvard Digestive Disease. Pooled donor human umbilical cord vascular endothelial cells, HUVECs (Lonza, Basel, CHE), were used at passage p2 to p6. Human primary hepatocytes (ThermoFisher Scientific Inc., Waltham, MA, USA). Human primary liver sinusoidal microvascular endothelial cells, LSECs (Cell Systems Corp., Kirkland, WA, USA). Primary human renal proximal tubule epithelial cells, RPTECs (ScienCell Research Laboratories, Carlsbad, CA, USA, cat #4100 and Lot (donor) 5110). CD34+ cells and stromal cells were isolated from whole blood and apheresis samples from human donors undergoing peripheral blood mobilization at the Massachusetts General Hospital.
Authentication	All cell lines were verified for typical morphology, expression of typical markers with immunocytochemistry, and/or functional assays.
Mycoplasma contamination	Mycoplasma testing was routinely done, and found to be negative in our cell-culture facilities.
Commonly misidentified lines (See ICLAC register)	No commonly misidentified cell lines were used.